

# Starshade Technology Development Activity Milestone 5A: Verify Petal Pre-launch Accuracy

Flora Mechentel, David Webb, Manan Arya, S. Case Bradford, Doug Lisman,  
*Jet Propulsion Laboratory, California Institute of Technology, Pasadena CA*

Eric Kelso, J. David Stienmier, Gregg Freebury, Andrei Iskra, and Amanda Swain  
*Tendeg, Louisville CO*

August 5, 2020

# Contents

<b>Executive Summary</b>	<b>2</b>
<b>1 Introduction</b>	<b>3</b>
<b>2 Starshade Flight Design</b>	<b>5</b>
<b>3 Petal Test Article</b>	<b>7</b>
3.1 Prototype Petal Design . . . . .	7
3.2 Prototype Petal Manufacture . . . . .	8
<b>4 Test Apparatus</b>	<b>9</b>
4.1 Thermal Chamber . . . . .	9
4.2 Furling Fixture . . . . .	10
4.3 Metrology . . . . .	11
<b>5 Experimental Approach</b>	<b>13</b>
<b>6 Data Analysis</b>	<b>14</b>
6.1 Data Processing Method . . . . .	14
6.2 Measurement Uncertainty . . . . .	17
<b>7 Discussion of Results</b>	<b>19</b>
7.1 Corrected Data . . . . .	19
7.2 Milestone Analysis . . . . .	21
<b>8 Conclusions</b>	<b>24</b>
8.1 Future Work . . . . .	24
<b>Acknowledgments</b>	<b>25</b>
<b>References</b>	<b>25</b>
<b>A Thermal Response of the MicroVu Measuring Machine</b>	<b>27</b>
<b>B First Environmental Testing Campaign</b>	<b>31</b>
B.1 Experimental Approach . . . . .	31
B.2 As-measured Data . . . . .	31
B.3 Temperature Correction . . . . .	32
B.4 Discussion of Results . . . . .	35
B.5 Summary . . . . .	37
<b>C Petal-width Bias</b>	<b>38</b>
<b>D Measurement Results: Width Change from Reference</b>	<b>45</b>
<b>E Measurement Results: Width Strain from Reference</b>	<b>46</b>

## Executive Summary

We present experimental results that meet the requirements of milestone 5A of the Starshade Technology Activity S5. Milestone 5A is concerned with the starshade petal subsystem. The 5A milestone definition submitted in 2018 allocated  $1.00 \times 10^{-11}$  instrument contrast to KPP5, which translated to the shape stability after thermal and deploy cycles needing to be consistent with a total pre-launch shape accuracy within  $\pm 70 \mu\text{m}$ . However, a new envelope value of  $\pm 95 \mu\text{m}$  was determined to produce the same instrument contrast and better represents the physical response of the actual hardware.

To address this milestone, a medium-fidelity prototype petal with shape-critical features was constructed. The petal was thermally cycled 50 times and deploy cycled to the stowage radius 5 times to experience the environmental conditions determined for the Starshade Rendezvous Mission (SRM). Over the course of testing, the in-plane petal shape was measured using a microscope-based measurement system (MicroVu Excel 250ULC). The width changes after environmental testing were calculated to determine the petal-width bias, i.e., the driver for optical performance of the starshade. We demonstrate compliance with S5 milestone 5A, with headroom to grow (100%) using conservative uncertainty bounds.

JPL and Tendeg jointly performed the design, analysis and fabrication of the test article, as well as of the thermal chamber and the furling fixture. Testing was performed at the Tendeg facility in Louisville, Colorado.

# 1 Introduction

This report details the S5 efforts to verify starshade petal pre-launch shape accuracy (KPP 5) and is intended to close out the S5 technology milestone 5A [1], which reads:

Petal subsystem with *shape critical features* demonstrates shape stability after deploy cycles and thermal cycles (deployed) consistent with a total pre-launch shape accuracy within  $\pm 70 \mu\text{m}$ .

The total allocation of contrast to KPP5 is  $1.00 \times 10^{-11}$ , and applies to the pre-launch petal shape. The  $\pm 70 \mu\text{m}$  was an initial estimate of the envelope value that would create the instrument contrast of  $1.00 \times 10^{-11}$ ; however, through the course of this activity, a new envelope value of  $\pm 95 \mu\text{m}$  was determined to produce the same instrument contrast, and better represents the physical response of the actual hardware. Table 1 shows that the requirement is sub-allocated to 1) manufacture, and 2) assembly, integration and test (AI&T) and storage before launch. For milestone 5A, we are only concerned with the AI&T and storage portion of this sub-allocation, which totals  $5.90 \times 10^{-12}$  with an envelope of  $\pm 83 \mu\text{m}$ , which is further sub-allocated to petal-width bias (global) of no more than 24 ppm ( $\pm 31 \mu\text{m}$ ), and petal-width bias (random) to 58 ppm ( $\pm 75 \mu\text{m}$ ), evaluated at the average petal width of 1.3 m. It should be noted that milestone 5A only demonstrates in-plane shape stability during AI&T, and that milestone 5B will also demonstrate stability during storage. Therefore, any headroom on the sub-allocation measured in milestone 5A may be utilized in part for variations in the in-plane shape due to storage.

Mission phase	Milestone	Sub-allocation term	ppm ( $\pm$ )	$\mu\text{m}$ ( $\pm$ )	Instrument contrast
Manufacture	5B	Edge segment shape	-	34	$1.84 \times 10^{-12}$
		Edge segment position (on petal)	-	30	$2.36 \times 10^{-12}$
		RSS / total	-	<b>45</b>	<b><math>4.20 \times 10^{-12}</math></b>
AI&T and storage	5A/5B	Petal-width bias (global) (do not exceed)	24	31	$5.31 \times 10^{-12}$
		Petal-width bias (random) ( $3\sigma$ )	58	75	$5.85 \times 10^{-13}$
		RSS / total	<b>63</b>	<b>83</b>	<b><math>5.90 \times 10^{-12}</math></b>
Pre-launch (Mfr,AI&T,storage)	-	RSS / total	-	<b>95</b>	<b><math>1.01 \times 10^{-11}</math></b>

Table 1: Sub-allocation of KPP5 concerning petal shape accuracy pre-launch. Milestone 5A is only concerned with AI&T and storage of the petal, and is a requirement in parts per million (ppm), where the change in width in  $\mu\text{m}$  is evaluated at the average petal width of 1.3 m. The manufacture sub-allocation is a maximum expected value and is based on demonstrated capability of a  $6 \text{ m} \times 2.4 \text{ m}$  prototype [2]. Unless otherwise specified, the contrast shown is the mean value for a normal distribution with the specified 3-sigma standard deviation of the engineering parameter. When a “do not exceed” value is listed, the contrast shown has been evaluated at the do-not-exceed value of the parameter.

The critical shape parameter of the petal is its width, i.e., the distance from one optical edge to the other. As utilized here, the term *bias* refers to the width error that is proportional to the petal width, and the *petal-width bias* portion of the error budget was established by considering the change in instrument contrast produced by petals of uniform width strain with respect to the nominal shape. To characterize the optical performance of a starshade with petals that have the same *non-uniform* width strain (along the petal length), it has been shown that the median width strain of the open lattice structure of the petal (e.g. the portion covered by battens and braces) is a metric that correlates very well to the petal-width bias. In other

words, a starshade with petals with realistic *non-uniform* width strains will produce very similar optical performance as a starshade with petals with a *uniform* width strain equal to the median width strain of the former. Using this metric to calculate the petal-width bias has been demonstrated in the context of thermal deformations for milestone 6A [3], and is repeated here in Appendix C.

For this milestone, the in-plane width variations of a sub-scale, medium-fidelity prototype petal with shape-critical features were measured after thermal and deploy cycles comprised in AI&T and storage. Because these environmental tests do not encompass *all* of the conditions experienced in this mission phase, growth margins with the requirement must be demonstrated to accommodate for other stressing environments. The petal width errors can be random from petal to petal, or global, meaning that they affect all the petals the same amount. The *random* error is a width bias on an individual petal, but not on the average width of the Starshade petals. The global error is a width bias common to all petals, and has a much larger effect on performance than the random errors. In other words, any individual petal may vary in petal-width bias by up to  $\pm 58$  ppm, so long as the average petal-width bias of the complete set of 24 petals is less than  $\pm 24$  ppm, and the distribution of those petal-width biases are uncorrelated.

Because only one prototype petal was built and tested for this milestone, there is no statistical sample set to calculate the random error sub-allocation and derive a  $3\text{-}\sigma$  deviation, therefore the requirement used here is the tighter *global* requirement of  $\pm 24$  ppm. This approach is consistent with a flight hardware selection process, in which components would be tested against performance criteria, and accepted or rejected for flight use. In conservatively constraining ourselves to this tighter requirement of global petal-width bias error, we gain confidence that the much looser requirement of random petal width error can be achievable for future programs. In other words, if each petal selected for the Starshade could be built to have a petal width bias below  $\pm 24$  ppm, the random petal width bias error of the set of 24 petals ( $\pm 58$  ppm) would be fulfilled by default.

A flight starshade will be designed to account for strain due to moisture loss in space. The corresponding source of shape error is the *uncertainty* in strain due to moisture loss (hygroscopic strain), but is not expected to drive performance, and is not characterized for milestone 5A at the petal level. However, hygroscopic strain is a possible source of noise for the work presented in this report. Coupon-level material testing for materials of the same CFRP resin system were characterized for a JPL flight program, and showed that the maximum variation in the battens would be 7.4 ppm, which represents the difference between a zero-moisture petal (on-orbit condition), and a petal soaked at 50% RH and 38 °C for 145 days<sup>1</sup>. The petal measurements for milestone 5A were collected over a short period of time (one month), where the relative humidity measured in the room remained between 10 and 20%. The effects of hygroscopic strain would therefore be a small fraction of the total possible strain of 7.4 ppm.

The petal shape was measured using a MicroVu Excel 250ULC metrology machine. An initial campaign of thermal and deploy cycles was performed, but the measurements showed large shape variations consistent with the thermal behavior of the machine (Appendix B). A second campaign of thermal and deploy cycles with measurements that produced more reliable results is presented in this report. For this reason, the initial shape of the petal before environmental testing cannot be compared directly to the final petal shape, but corrections of the data from the first campaign strongly suggest exceedingly small width changes compared to the requirement. Initial shape change will be characterized for milestone 5B. Additionally, any significant initial shift in shape would be characterized and accounted for in the design.

This document is organized as follows. Section 2 describes the starshade mechanical design and subsystems; Section 3 provides details on the medium-fidelity prototype petal that was used for this investigation; Section 4 describes the hardware used for thermal and deploy cycles, as well as the metrology system for petal measurements; Section 5 gives the experimental approach and the timeline of events; Section 6 presents the data post-processing methods employed to establish the true petal width change and its conservative uncertainty. Finally, Section 7 provides the results of this campaign and compares the key performance parameter to the milestone requirement.

---

<sup>1</sup>Data available upon request.

## 2 Starshade Flight Design<sup>2</sup>

The Starshade is a deployable structure that has three subsystems: the inner disk, the petal, and the petal launch restraint and unfurl subsystem (PLUS), shown in Figure 1. The petals and truss are designed to be deployed independently, in a two-phase deployment. First, the PLUS quasi-statically releases the petals from their furled (launch) condition; then, the truss launch locks are released; finally, the truss deploys the petals to their design diameter.

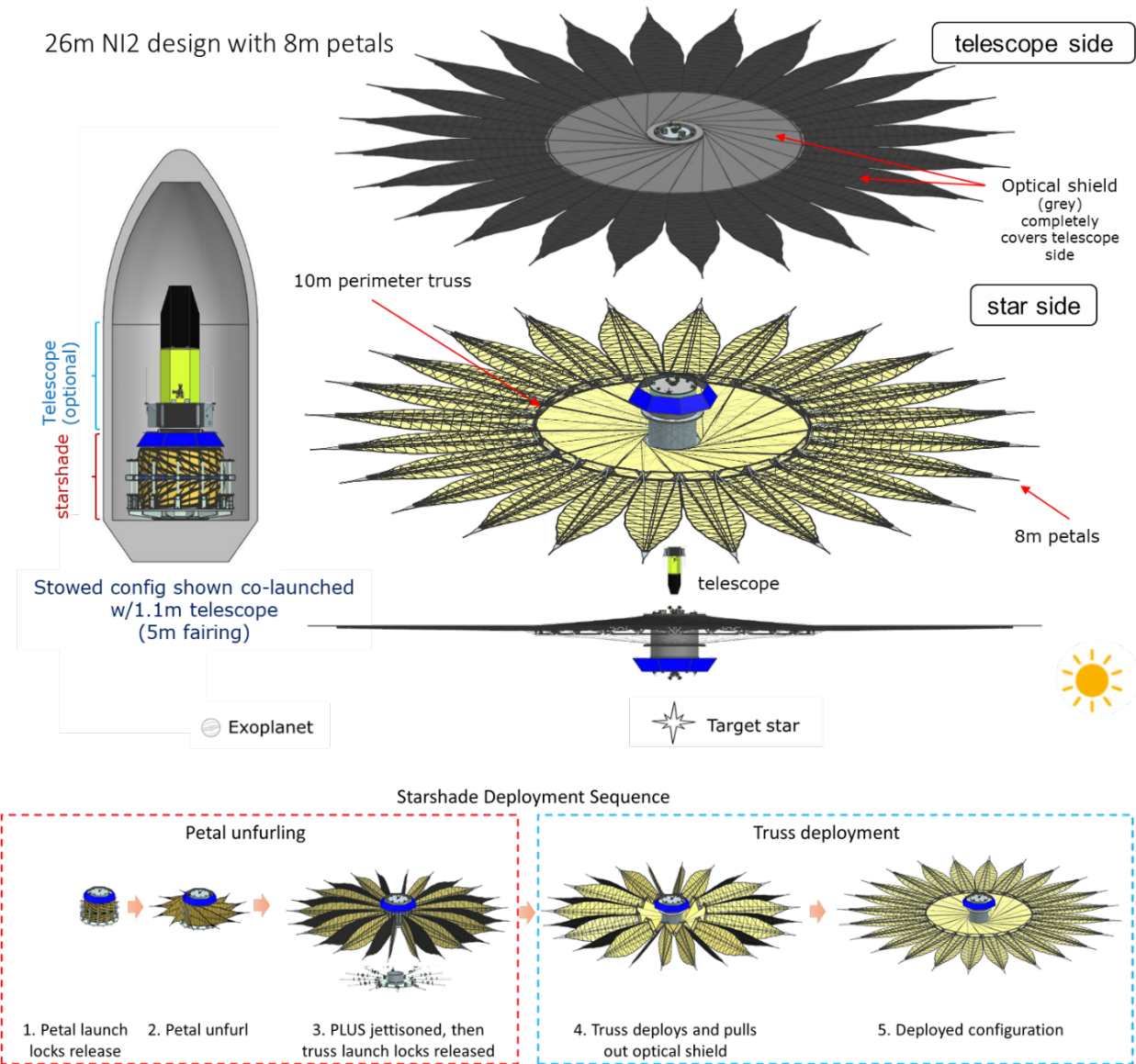


Figure 1: Starshade mechanical system including deployed and stowed configuration with relative position of starshade, telescope and star (top). Deployment sequence for the starshade, beginning with petal unfurling, and completing with deployment of the perimeter truss (bottom).

The petal subsystem is designed to be stiff in-plane to maintain the precise shape of the edge. This is important on the ground during manufacture, test, and launch. It is accomplished with a repeating

<sup>2</sup>The content of this section has already been described in the Starshade Technology Development Activity Milestone 6A Report [3], and is repeated here for clarity. For a more detailed description of all starshade subsystems and the deployment sequence, see the Probe Study [4] and HabEx reports [5].

doublet of triangular trusses formed by the battens, braces, center spine, and optical edge. The design of the petal—shown in Figure 2—is a result of analysis that showed the petal would be sufficiently stiff in-plane to maintain its shape through ground handling for verification after environmental testing. The batten spacing increases from root to tip, and is dictated by the petal furling radius. The petals are positioned and attached to the truss with three hinges at the root of the petal; the center hinge is responsible for lateral location, and the edge hinges are allowed to slip in the hinge axis, so as not to over-constrain the petal. The petal is restrained out-of-plane with two struts that connect down from the truss nodes to the bases of the two out-of-plane ribs, which run from the root corners of the petal out to the tip. Because the petal is hinged at the root, the strut provides the additional out-of-plane constraint needed to set the petal in the plane of the starshade. The ribs are hinged along the length of the petal, providing the the out-of-plane stiffness needed to maintain the planarity of the petal, which is a loose requirement, at multiple centimeters at the tip. The ribs are maintained out-of-plane with a series of small struts from the rib down to the petal, which forms a small triangular truss between the rib-strut-batten. The rib is piano-hinged along its length at its connection to each batten, and is free to slide along this hinge so as to not over-constrain the rib to the petal. For stowage, the ribs rotate down, which allows the petal to wrap around the central hub. A small spring in the rib strut, combined with the rib’s over-center hinge, deploys the rib on-orbit. The petal is restrained in the launch condition at the cart assemblies along the central spines at every other batten, which provide a rigid interface to preload the stack of petals for launch, without imparting large loads into the individual petals. The petal optical shield covers the entirety of the telescope side of the petal, but is loosely connected to the structure so that it does not impart any load from thermal deformation. The flight petal design for the SRM is 8 m long, with a maximum width of 2 m. The average width is 1.33 m wide, which is roughly the same as the 1.33 m-wide root of the petal, where it interfaces with the truss.

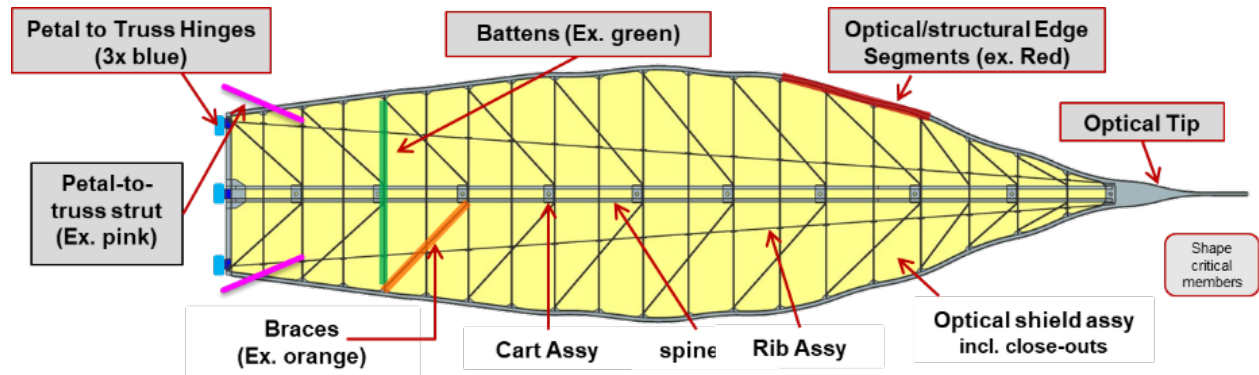


Figure 2: Flight petal design.

Overall stiffness is achievable because the CFRP with which the petals are constructed has a high stiffness-to-mass ratio. The battens are specifically selected to be a uniaxially pultruded carbon fiber/epoxy matrix, providing for an adjustable rod that has very consistent material properties across a production lot of hundreds of meters. The braces are made from a similar pultruded rod of a thinner cross section to allow it to furl with the petal. The spine and edge are an M55J-cyanate ester laminate that allows the coefficient of thermal expansion (CTE) to be accommodated, while also providing strength for interfacing to the petal launch tie-down cart assemblies. Ultimately, material property characterization, model validation, and thermal environment refinement iterations optimize the exact pultrusions and laminate layup that will be used for the flight design, and are all adjustable parameters.

### 3 Petal Test Article<sup>3</sup>

#### 3.1 Prototype Petal Design

To evaluate the pre-launch shape stability of the petal, a sub-scale prototype test article was built by JPL and Tendeg. The prototype petal is flight-like in terms of all component cross-sectional dimensions and materials, but is 3/4-scale in terms of the overall assembly width and 1/2-scale in terms of overall assembly length. The reduced dimensions support the use of available facilities. Not included in the prototype petal are the optical shield and the pop-up ribs, which do not participate in shape maintenance; however, these will be included in milestone 5B to improve prototype fidelity. It included the critical features for mechanically and thermally induced deformation performance. For the test article to be most relevant to the flight design, the prototype petal was designed to very closely match the driving structural characteristics of the flight design, including component materials, cross-sectional dimensions, joint geometry and adhesive, and overall structure geometry. The thickness of the prototype petal and the cross-section of all components were maintained.

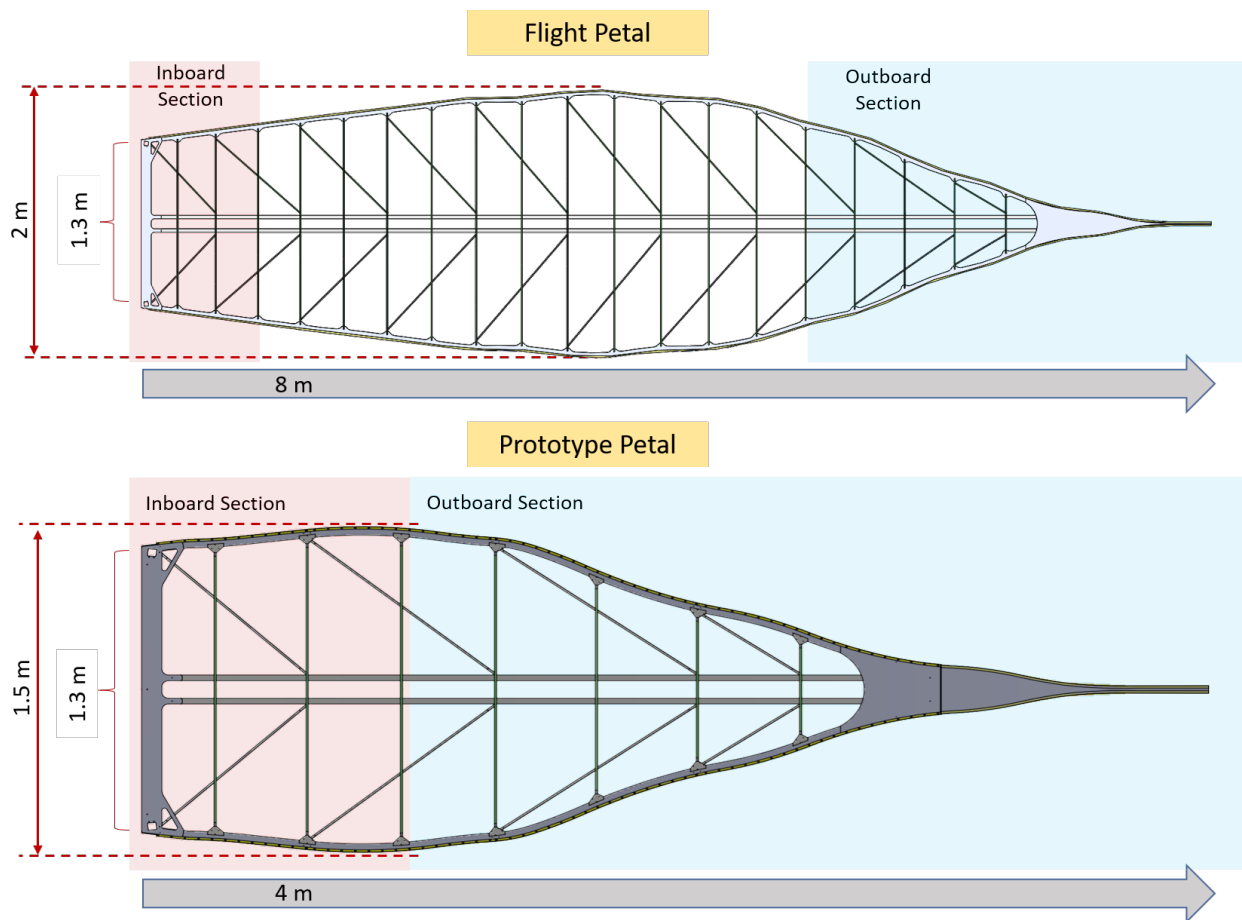


Figure 3: Prototype petal juxtaposed with the flight petal.

The two critical parameters for petal-width performance are the material properties and the shape-critical components that create the triangular trusses of the petal in-plane shear structure. The design of the prototype petal focused on maintaining these two parameters with respect to the flight petal. Figure 3 illustrates the methodology for designing the prototype petal based on the full-scale flight design, showing that the prototype is a conjoining of the inboard and outboard sections of the flight design, and smoothed

<sup>3</sup>The content of this section has already been described in the Starshade Technology Development Activity Milestone 6A Report [3], and is repeated here for clarity.

out at the transition. The result was a prototype that maintained the end-conditions of the flight-petal at the root and tip, and also contained a large section with repeating triangular trusses that create the structure of the petal. This allows for a fairly direct cross-correlation of the two models, as well as a general traceability of the design. The cross-sectional geometry of each component of the prototype petal is also identical to that of the flight design. The prototype petal is of medium fidelity in materials and shape-critical components, but does not contain features that do not drive petal shape, e.g. the optical shield, out-of-plane ribs, and cart assemblies outlined in Section 2; the milestone 5B petal will include these features. Because the MicroVu metrology system (Section 4.3) has a total measurement area of  $2.5 \times 1.6$  m, the prototype was constrained to a max width of 1.5 m.

### 3.2 Prototype Petal Manufacture

A main objective for the production of this prototype was to maintain traceability to the flight manufacture process, so that the results could be applicable to future programs. To that end, the same materials as for the notional flight petal—described in Section 2—were used. The components of the petal were hand-laid M55J carbon fiber laminates for the optical edge, spines, root, and tip, and machine-drawn uniaxially pultruded carbon fiber-epoxy rods for the battens and braces. Flight-grade EA9394 epoxy was used to bond the components together at room temperature. The assembly process was performed in a flight-like fashion, with special care taken to achieve as close-to-nominal geometry as possible, to mitigate these as sources of error between the as-built hardware performance and the prediction. The principal concern was offsets in hardware geometry, which could cause moments internal to the structure, and adhesive thickness in joints, because the epoxy makes a significant contribution to local joint thermal strain. To that end, the petal manufacture was performed on optical benches and laid out with a combination of custom manufacturing tooling and off-the-shelf linear stages, visible in Figure 4. The tooling was laid out with a portable coordinate measuring machine (CMM) Faro Arm. The structure of the petal before the optical edge installation is not required to have the same accuracy as the optical edge profile, so this process was sufficiently accurate for the structural layout of the petal. It is worth noting that this test article was also used to satisfy milestone 6A by demonstrating shape stability at temperature. Milestone 6A was completed before the thermal and deploy cycling used to satisfy Milestone 5A.

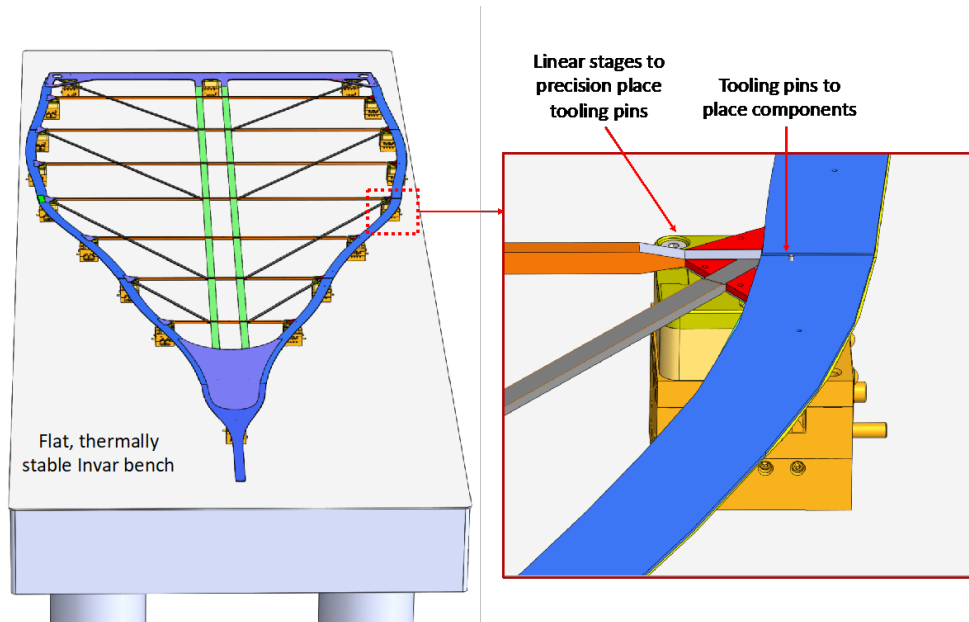


Figure 4: Representation of the fixture used for the prototype petal manufacture. Right detail shows a linear stage used to align the pins that held the components in the correct location during bonding.

The optical-edge foil was bonded to the CFRP laminate substrate in analogous fashion to that performed

for milestone 3. However, although the edges of the prototype petal used for milestone 5A were chemically etched, they are not required to meet solar scatter requirements, and no measurements were taken. The edge segments were then bonded to the petal structure in sequential fashion from root to tip. The placement of the edges is only as accurate as the tooling, because the milestone 5A prototype petal is not required to meet the manufacturing shape accuracy that the milestone 5B petal will demonstrate. Figure 5 shows the as-manufactured petal atop the tooling used to assemble it. A flat, thermally stable Invar bench was key in providing a stiff and stable structure on which the tooling could be accurately placed. A major concern was ensuring that the petal was flat when bonded, and that all the components were strain-free when laid out, in order to minimize residual stresses in the petal after bonding the components together. The precision tooling supported the structural edge of the petal within  $\approx 0.25$  mm flatness across the structure while the joints and edges were being bonded.

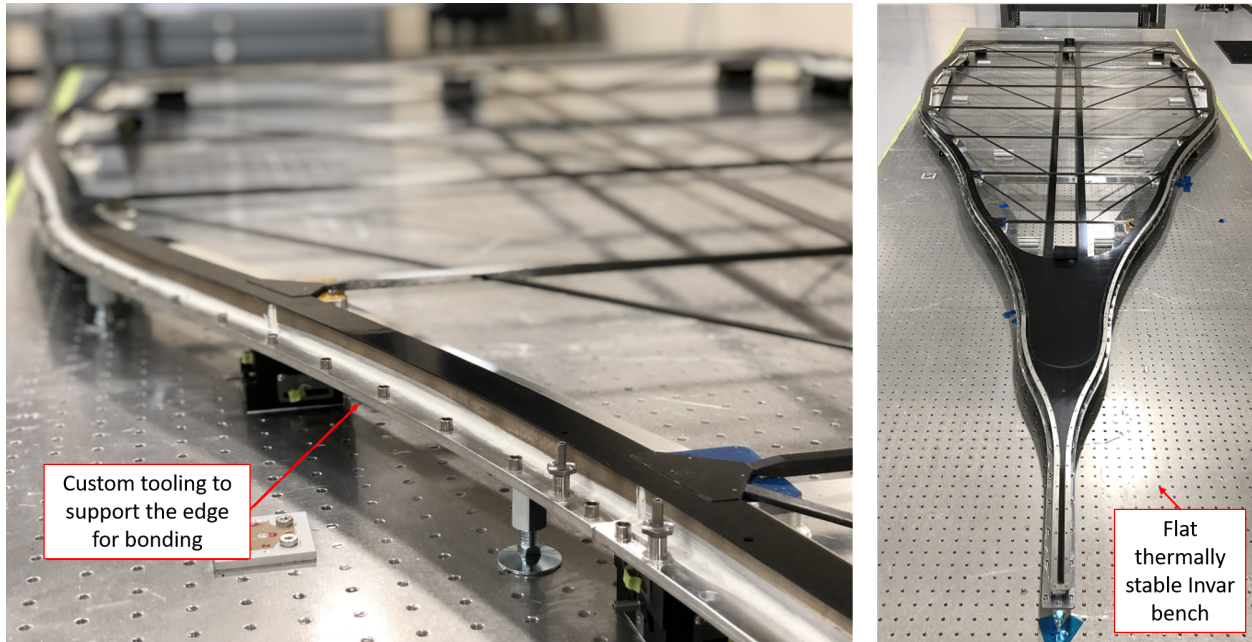


Figure 5: As-manufactured petal completed and sitting on manufacturing tooling that allowed precision placement of all components, and precise epoxy bonding. Left image shows petal with the telescope side down. Right image shows the petal telescope side up, with about 12 mm of the edge foil showing.

## 4 Test Apparatus

### 4.1 Thermal Chamber

A custom-built thermal chamber was built for the needs of milestones 5A and 6A, and connected with a duct to a Cincinnati Sub Zero (CSZ) ZPS-64-6-6-SC/WC chamber used for milestone 7A. The foam box uses a diffusing mesh in the lid with multiple channels to allow air to flow sideways along the top of the chamber. Additionally, multiple fans were placed inside the box to force air recirculation and achieve a uniform thermal distribution around the test article. Thermocouples were placed in the chamber for monitoring. The ramp rate was on the order of  $1.3^{\circ}\text{C}/\text{min}$  for the 50 cycles performed, with minimum and maximum temperatures of  $-50^{\circ}\text{C}$  and  $+50^{\circ}\text{C}$ . The minimum temperature was limited by the capabilities of the thermal chamber system. A picture of the petal installed in the thermal box is shown in Figure 6.

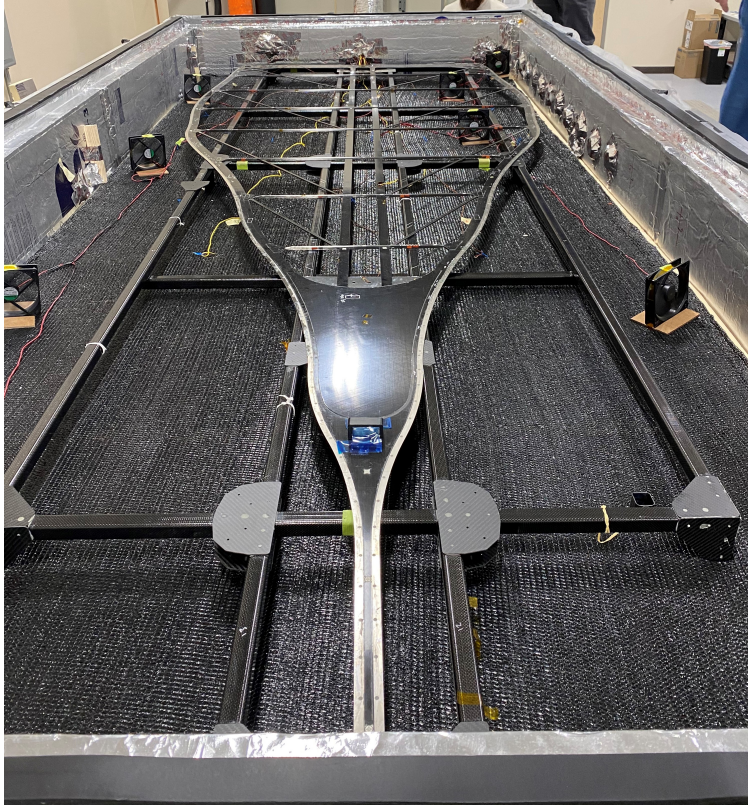


Figure 6: Prototype petal installed in the thermal chamber (with the lid removed). The diffusing mesh in the lid is the same as the black mesh under the petal.

## 4.2 Furling Fixture

A custom fixture was built for the purposes of furling the prototype petal to the stowage radius of 1.125 m. The petal is wrapped around a wooden drum, with care taken to not have any load applied to the optical edge. The petal was restrained to the drum with straps that ran over the petal interface locations for launch (on the battens) and the straps were tensioned by weights over pulleys. The furling movement was operated manually and completed a total of 5 times before remeasuring the petal. A picture of the petal fully furled on the fixture is shown in Figure 7.



Figure 7: Prototype petal installed on the furling fixture.

### 4.3 Metrology

A MicroVu Excel 250ULC machine was used to measure the prototype petal width at the terminal edge. The MicroVu consists of a microscope mounted on an  $(x, y)$ -translation stage. Images from the microscope are used to extract the 2D location of edges of parts. To know the  $(x, y)$  location of the microscope, the machine uses two orthogonal Renishaw RGS40 gold-plated steel linear encoders [6]. These encoder strips are bonded to a substrate: along the  $x$ -axis the substrate is the granite bench, and along the  $y$ -axis the substrate is a steel bar. The machine has a stated accuracy of  $(5.5 + L/300) \mu\text{m}$ , where  $L$  is a part length expressed in millimeters. The  $5.5 \mu\text{m}$  term is derived from measurement repeatability, and the  $L/300$  term encompasses all length-dependant errors, but is mainly driven by the thermal strain of the MicroVu machine itself. As the temperature of the granite and steel substrates changes, thermal strain of the substrate translates to thermal strain of the linear encoders, introducing length measurement errors.

Unfortunately, MicroVu does not currently compensate for the thermal strain of the device by default<sup>4</sup>. As a result, to post-process the data and correct for the error in width due to environmental temperature changes, the MicroVu was instrumented with 6 high-accuracy ( $\pm 0.15 \text{ }^\circ\text{C}$  absolute,  $\pm 0.01 \text{ }^\circ\text{C}$  random error) resistance temperature detectors (RTDs), one on each corner of the granite bench (longitudinal  $x$ -axis), and one on each end of the steel gantry (width-wise  $y$ -axis). Appendix A describes the experimental characterization of the coefficients of thermal expansion of the linear encoders, measured as  $CTE_x = 4.9 \text{ ppm}/^\circ\text{C}$  in the  $x$

<sup>4</sup>Based on communications with MicroVu representatives. MicroVu software includes a non-default option to correct for encoder thermal strain using an operator-supplied MicroVu-internal temperature. However, this option was not discovered until partway through this work, and was not used moving forward to maintain consistency and continuity of measurements. Moreover, this option requires the operator to measure and supply a MicroVu-internal temperature; the capability to measure this temperature was not developed until after this work. MicroVu representatives have indicated that future MicroVu models currently under development will include internal thermometers to enable automatic compensation for encoder thermal strain.

direction and  $CTE_y = 11.2 \text{ ppm}/^\circ\text{C}$  in the  $y$  direction. The complete data post-processing method of the petal is described in Section 6.

The maximum measurement area of the MicroVu is 2.5 m in the  $x$  direction (longitudinal) and 1.6 m in the  $y$  direction (width). Since the prototype petal measures over 4 m in length, two sets of measurements were required to define the complete petal width along the longitudinal axis. The “base” scan covers the petal from the root—interfacing with the truss—to the 7<sup>th</sup> (and last) batten (approximately 1 m from the end of the tip). The “tip” scan covers the petal from the 7<sup>th</sup> batten to the very end of the tip. Fortunately, the base scan alone captures the terminal edge along the entirety of the batten-portion of the petal, which is the portion of interest for width change driving optical performance. The fixture for the petal was designed to minimize out-of-plane deflections and stiction to provide a repeatable measurement platform. Pictures of the prototype petal installed on the MicroVu are shown in Figure 8.

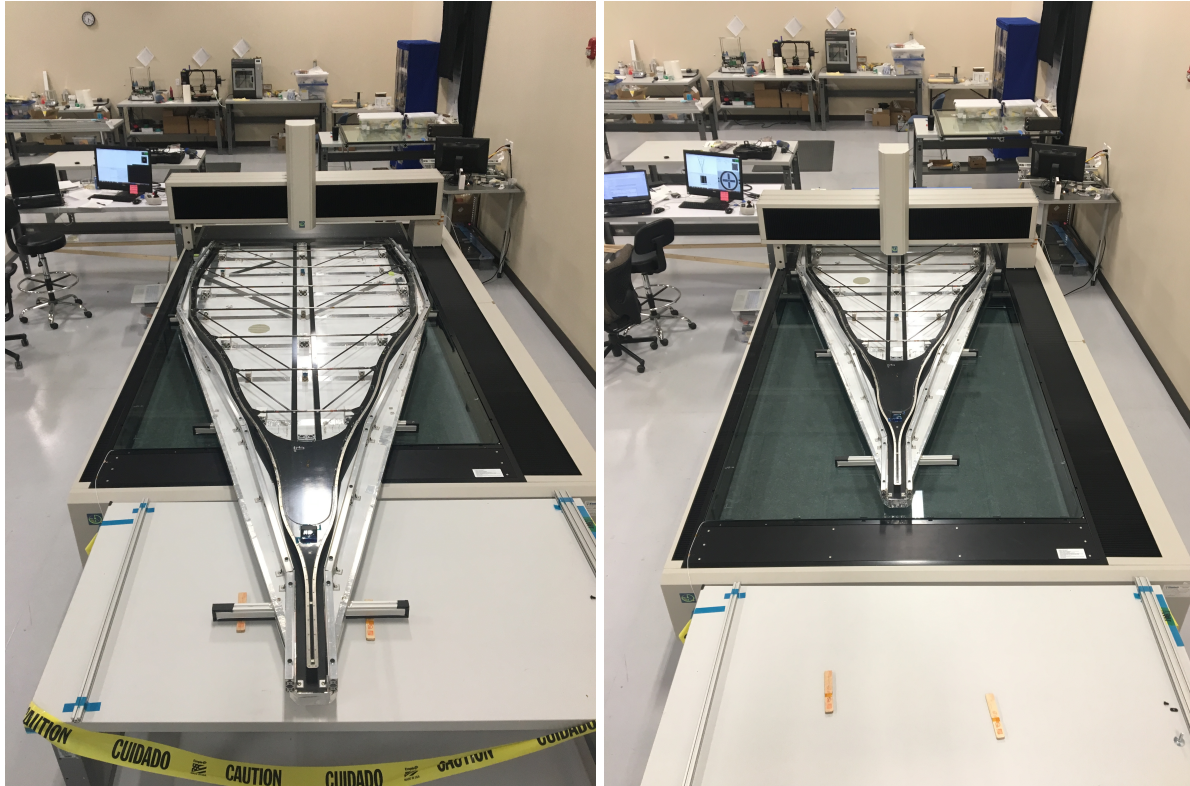


Figure 8: Prototype petal installed on the MicroVu for the base scan (left) and the tip scan (right).

To easily compare separate data sets, a local coordinate system is established using four optical targets (3.3 mm circles with crosshairs) each bonded to a batten, along the centerline of the petal. The microscope first captures the position of these four optical targets (on battens 4, 5, 6, and 7 numbered from the root) that are common to both the base and tip scans. The best-fit skew line between these four targets defines the local longitudinal axis of the petal, and the optical target on batten 6 defines the  $(x, y)$  origin. Each optical edge is defined with a series of 1 mm-windows, spaced 2 cm apart, and containing approximately 100 edge points. To locate an edge, the MicroVu software looks for areas of high contrast change on the microscopy images (dark to bright). The sharpness of an edge on the image can be modified with the variety of lighting options that the MicroVu offers. An snapshot of a single measurement window on the optical edge foil is shown in Figure 9, as can be seen on the MicroVu user interface. The points on the edge determined by the image processing software are shown in blue.

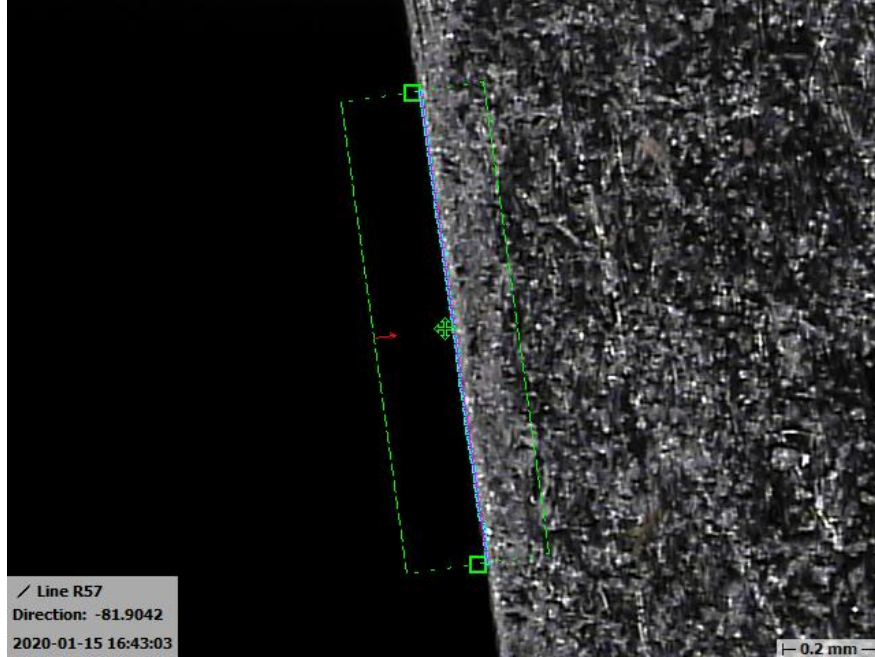


Figure 9: 1 mm-wide MicroVu measurement window (defined in green) of the metal foil forming the optical edge, containing approximately 100 points (blue). The 185 measurement windows are spaced approximately 2 cm apart.

## 5 Experimental Approach

All testing was performed at the Tendeg facility in Louisville, Colorado. After a baseline measurement of the petal (base and tip) was captured, the prototype petal was thermally cycled in the custom environmental chamber (described in Section 4) between  $+50\text{ }^{\circ}\text{C}$  and  $-50\text{ }^{\circ}\text{C}$ . The temperature range was defined by the mission parameters discussed in Section 1. In the context of milestone 6A [3], FEM analysis showed that the batten displacements have the largest effect on width change of the petal. The maximum on-orbit temperature occurs during retargeting, corresponding to a maximum average batten temperature of  $69\text{ }^{\circ}\text{C}$  at a sun angle of  $0^{\circ}$ , and to a minimum average batten temperature of  $-60\text{ }^{\circ}\text{C}$  at a sun angle of  $83^{\circ}$ . Batten and epoxy CTE testing showed no change in behavior of the material properties between  $\pm 50\text{ }^{\circ}\text{C}$  and the greater on-orbit operational temperature range, mitigating concern of the abbreviated test temperature range limited by the available facilities and system setup.

The number of thermal cycles for the prototype petal was derived from the number of thermal cycles in the deployed configuration for the Starshade Rendezvous Mission (SRM), i.e., the reference mission for the S5 technology development. It is based on the number of target star re-orientations, a maneuver which results in the starshade changing orientation with respect to the sun, and thus cycling the temperature of the starshade. For milestone 5A, the petal was thermally cycled 50 times, and measured every 10 cycles. Because the starshade petal is nominally unloaded on orbit, the prototype petal was tested in an unloaded configuration as well. Deploy cycles for a flight petal could be as many as 10 during AI&T, and of course 1 after launch. For milestone 5A, the petal was cycled 5 times, then remeasured. Milestone 5B will perform an additional 5 cycles and remeasure. Future work in the context of Milestone 5B will characterize the complete life cycle of the petal. The petal was transported between the MicroVu and the thermal chamber/furling fixture with a custom rig that supported the structure at the battens. The measurement fixture that the petal rested on during the MicroVu measurements was never placed in the thermal chamber.

After collecting the baseline results, petal measurements were only taken when the MicroVu temperatures were close to the temperatures measured during the baseline measurement. For a petal measurement to be taken, the temperature of the granite substrate had to be within  $\pm 1\text{ }^{\circ}\text{C}$  of the baseline temperature, and the temperature of the steel substrate within  $\pm 0.6\text{ }^{\circ}\text{C}$  of the baseline. In addition, low-CTE ( $0.13\text{ ppm}/^{\circ}\text{C}$ )

carbon fiber-epoxy rods were used as “truth bars” to serve as an additional verification method. Because any thermal deformations of these rods at ambient temperature (less than 1  $\mu\text{m}$ ) were below the MicroVu measurement capabilities, any measured differences in lengths of the rods were attributed to thermal strain of the MicroVu encoders. The rods were measured before and after each petal scan, and the rod length differences had to be below  $\pm 10 \mu\text{m}$  ( $\approx 7$  ppm) from the baseline. This was done to minimize the error in the non-corrected, as-measured petal data.

The thermal behavior of the MicroVu was not taken into account during the measurements in the first environmental testing campaign, carried out between March and September 2019. As a result, petal width changes during this first campaign coincided with  $\pm 3^\circ\text{C}$  temperature swings in the room, which were indistinguishable from the actual shape change because the temperature of the encoders was not taken during that period. These preliminary results and an effort to correct the data for thermal effects are given in Appendix B. After instrumenting the MicroVu with RTDs and characterizing its thermal behavior, a second environmental campaign was carried out between January and February 2020. The complete set of data for milestone 5A therefore includes the 7 different conditions of the second campaign, listed in Table 2 with the respective measurement dates. The temperature measurements of the MicroVu were used in the data post-processing and uncertainty estimation to obtain more accurate results. For the remainder of this report, a *condition* refers to the state at which the petal was measured, i.e., after  $n$  thermal or deploy cycles.

Measurement date	Condition	Data reference name
2020.01.15	Baseline	Baseline
2020.01.17	10 thermal cycles complete	Post10TC
2020.01.21	20 thermal cycles complete	Post20TC
2020.01.24	30 thermal cycles complete	Post30TC
2020.01.27	40 thermal cycles complete	Post40TC
2020.02.04	50 thermal cycles complete	Post50TC
2020.02.12	5 deploy cycles complete	PostFurl

Table 2: Petal testing and measurement timeline for the second environmental campaign.

## 6 Data Analysis

### 6.1 Data Processing Method

In the following analysis, the  $x$ -axis corresponds to the longitudinal axis of the petal, and the  $y$ -axis corresponds to the width-axis of the petal. In practice, the longitudinal axis of the petal is defined as the best-fit line through optical targets bonded to four battens, as described in Section 4.3, and shown in Figure 10. After this stage, all measurement outputs are in this local petal coordinate system, and not in the absolute MicroVu machine coordinate system. A total of 185 windows, roughly 2 cm spaced apart, are captured on each edge to define the petal shape, with 122 taken from the base scan and 63 from the tip scan. Each individual 1 mm-wide window (Figure 9) contains approximately 100 points, spaced  $\approx 10 \mu\text{m}$  apart. The main limitation in sampling frequency is the measurement time needed. About 40 minutes were required to acquire 185 petal widths with the MicroVu, a period of time over which the machine temperature must remain very stable. The width strain over the open-lattice structure as a function of  $x$  can be decomposed into components of different spatial frequencies (in cycles per petal). The instrument contrast is most sensitive to components with frequencies less than 5 cycles per petal, and components above 10 cycles/petal have been shown to have minimal effects on contrast. The batten displacements have the largest effect on petal width and the batten spatial distribution of the prototype petal is roughly 7 cycles/petal. As a result, the component of largest amplitude in the spatial decomposition of the prototype petal width strain is expected to be 7 cycles/petal. Because 130 windows cover the open lattice structure of the petal, this sampling

frequency corresponds to a largest measurable spatial frequency of 65 cycles/petal, so that the components that have the largest effect on instrument contrast are well resolved with the selected sampling frequency.

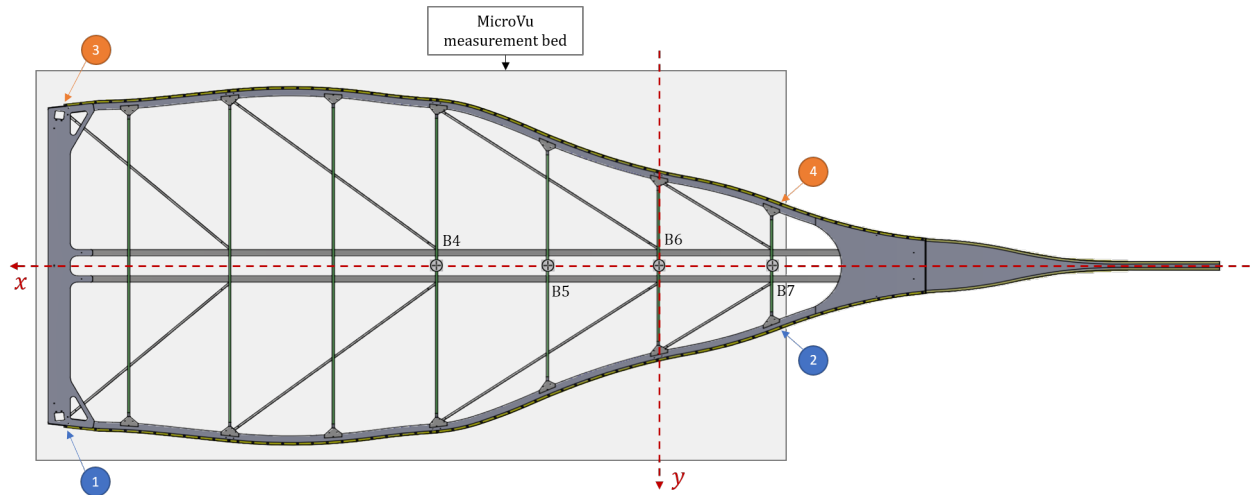


Figure 10: Schematic of the prototype petal on the MicroVu bed for a base scan, covering the petal from the root to the 7<sup>th</sup> batten. The local coordinate system is defined using optical targets located on battens 4, 5, 6, and 7 (labeled B4–7). The origin is established at B6. The program captures 1 mm-wide windows on one edge (between points 1 and 2), then on the other edge (between points 3 and 4). Optical targets on this image are not to scale.

To correct for the thermal behavior of the MicroVu, the data is first all aligned to reference  $x$  coordinates, and then corrected for thermal strain in both  $x$  and  $y$  directions.

The  $x$  positions of the centers of each window recorded on the first edge of the baseline scan are taken as the *reference* coordinates for the second (opposing) edge of the petal, and for both edges of all subsequent conditions. The petal widths are only compared at these 185 discrete  $x$  locations. The next step is to determine the  $y$  coordinate on the edge at the reference  $x$  location. To do so, a linear fit is applied to each window using the  $\approx 100$  collected points. The average of the standard deviations of the residuals from this linear fit were below  $2\ \mu\text{m}$  across all conditions, driven by the imperfect straightness of this small section of edge, but mostly by the precision of the image processing software. In particular, dust, scratches or roughness on the optical edge can produce areas of high contrast which can be picked up as the terminal edge. Figure 11 shows two MicroVu snapshots of extreme cases to illustrate this point, with the outline of the window in green, the point cloud in blue, and the best fit line in purple.

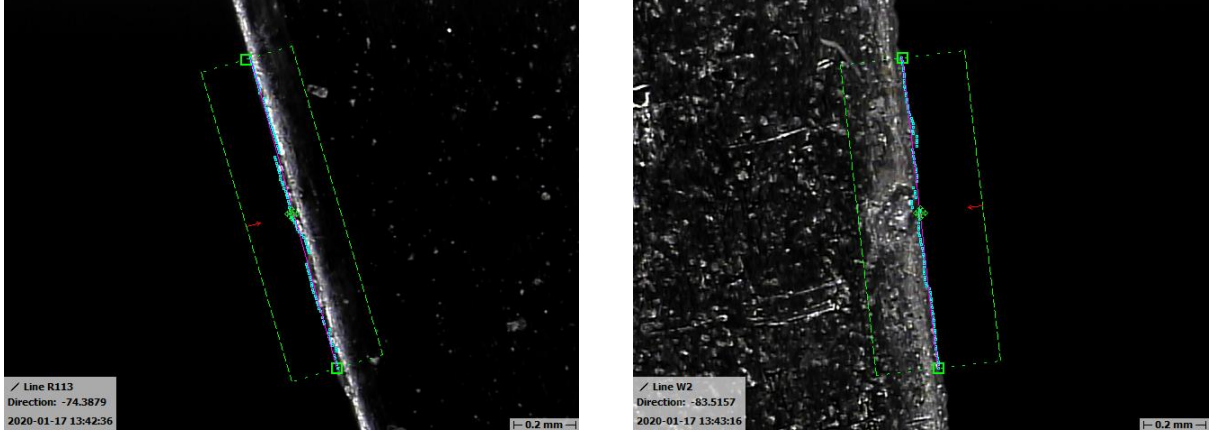


Figure 11: Snapshots of petal edges showing large residuals with respect to a linear fit applied to a 1 mm measurement window. The purple line is the linear fit, and the individual blue points are the locations of high contrast established by the MicroVu image processing software. The two images are taken from measurements on opposing edges.

With a local linear equation ( $y = ax + b$ ) established in each window, the  $y$  coordinate along the edge of petal can be derived at the reference  $x$  locations ( $x_{ref}$ ) taken from one edge of the baseline scan. This is important for two reasons: the position that the MicroVu’s microscope is commanded to measure at ( $x_1$ ) has some repeatability error, and the measurement windows on one edge can deviate slightly from the windows on the other edge. Realigning all the data to a set of reference  $x$  positions corrects for small differences in measurement window location.

Furthermore, the reference measurement location is affected by changes in temperature from the baseline ( $\Delta T$ ) due to machine encoder thermal displacements. To account for thermal effects in the  $x$ -axis, the  $y_2$  coordinate of the edge is actually evaluated at a *corrected*  $x_2$  location, using Equation (1). To illustrate this, consider a petal measurement taken at a warmer temperature than that of the baseline scan. The MicroVu software commands the microscope to capture the edge at a hard-coded  $x$  location ( $x_1 = x_{ref}$ ). But because the encoder on the granite bed has thermally expanded, the microscope will travel further than it did for the baseline scan, and the  $x$  location that corresponds to the same position of measurement is actually  $x_2$ .

$$\begin{cases} x_2 = \frac{x_1}{1 + CTE_x \cdot \Delta T} \\ y_2 = ax_2 + b \end{cases} \quad (1)$$

The third step is to correct each  $y$  measurement on the edges for the machine thermal strain of the  $y$ -axis using Equation (2).

$$y_3 = y_2(1 + CTE_y \cdot \Delta T) \quad (2)$$

Finally, the petal width is the difference between the corrected  $y$  coordinates on each edge of the petal; width is shown in Figure 12, with the root redefined at  $x = 0$  for clarity. The red plot (right axis) shows the slope of the width, which is relevant when considering the error in width due to any error in  $x$  position.

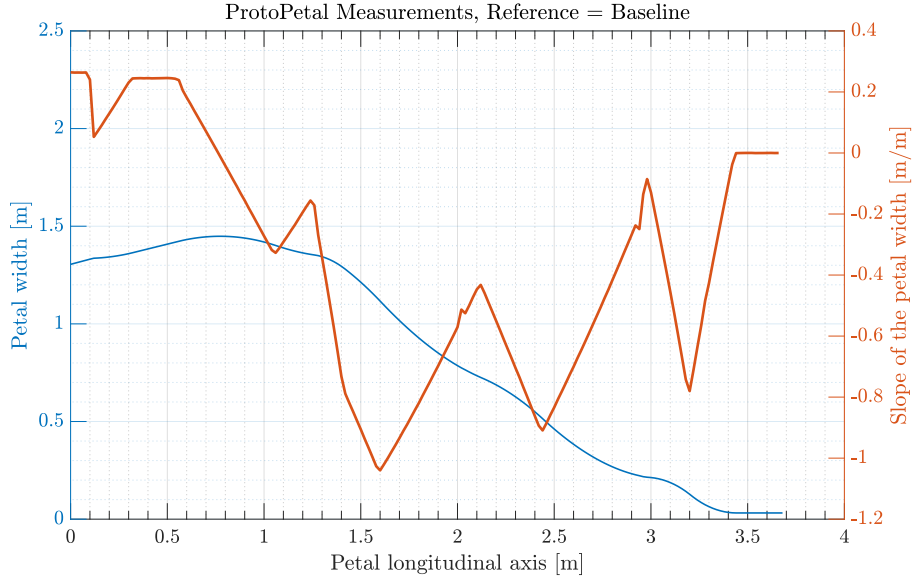


Figure 12: As-measured petal width in blue and slope of the width in red, along the longitudinal axis with the tip to the right.

To summarize, the data collection and processing steps at a condition after the baseline are the following:

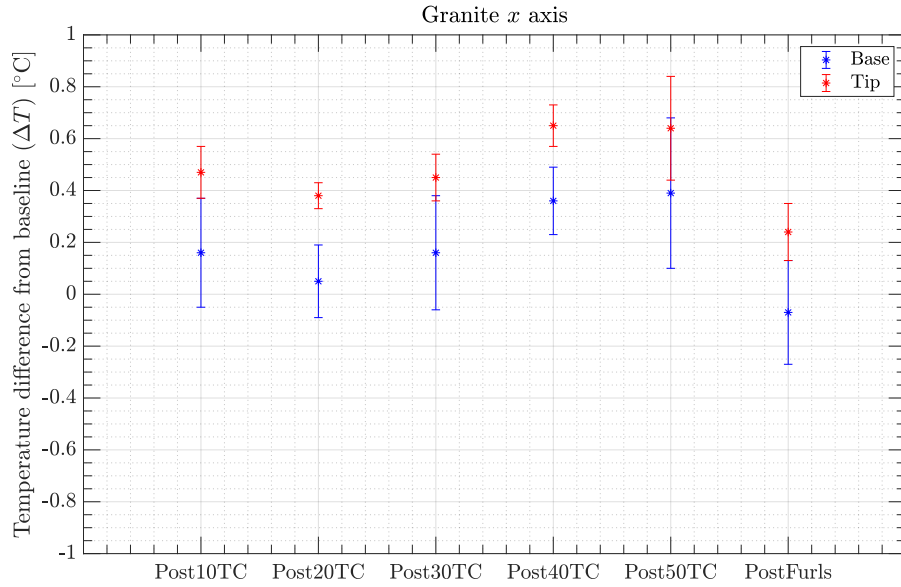
1. Define a local petal coordinate system using measurements of 4 optical targets. This best-fit skew line sets the midline axis of the petal to which the measured widths are perpendicular.
2. Capture 1 mm-wide windows spaced 2 cm apart on each edge. Each measured window contains roughly 100 points. The petal shape is defined with 185 windows.
3. For each measurement window, define a local linear fit using  $\approx 100$  points.
4. On each edge, calculate  $x_2$ , the corrected measurement location that corresponds to the baseline measurement location, accounting for thermal strain of the MicroVu on the x-axis.
5. On each edge, calculate the  $y_2$  coordinate on the edge at the  $x_2$  position using the local linear fit.
6. Calculate  $y_3$  to correct  $y_2$  for thermal strain of the MicroVu on the y-axis.
7. Calculate the width of the petal at  $x_{ref}$  by taking the difference of the corrected  $y_3$  measurements on each edge.

## 6.2 Measurement Uncertainty

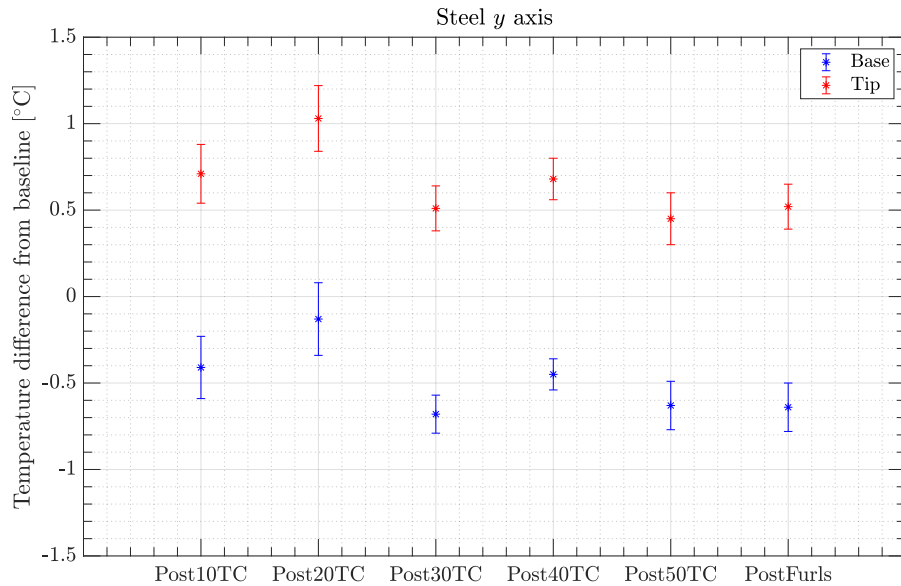
As mentioned in Section 4.3, the  $(x, y)$  measurement accuracy on the specification sheet of the MicroVu Excel 250ULC machine is  $(5.5 + L/300) \mu\text{m}$ , where the  $L/300$  term is mainly attributed to thermal effects of the machine, and  $L$  is a part length expressed in millimeters. To correct the measured data for temperature variations, the thermal response of the MicroVu was characterized by measuring the CTEs of each axis (Appendix A), providing empirical values for  $CTE_x$  and  $CTE_y$  used in Equation (1) and Equation (2).  $\Delta T$  is the temperature difference from the baseline scan.

The uncertainty related to the thermal correction described in the previous section is driven by the uncertainty in determining  $\Delta T$ . A single  $\Delta T$  value for a condition is calculated by averaging the temperature over the measurement time, and averaging the  $\Delta T$  values between different sensors (4 on the  $x$ -axis and 2 on the  $y$ -axis). The RTDs have a  $\pm 0.15^\circ\text{C}$  absolute error, which is a constant bias for each sensor that could be reduced with calibration. However, because we are only considering changes in temperature over time, the absolute error is subtracted. Figure 13 shows the temperature variations for each measured condition (on

both axes) with their respective error bars, i.e., a root-sum-square of the error due to temporal averaging and the error due to averaging between multiple sensors.



(a) Temperature variations between conditions measured on the granite  $x$ -axis.



(b) Temperature variations between conditions measured on the steel  $y$ -axis.

Figure 13: Temperature variations between a given condition and the baseline scan for both the granite and steel axes, and for the base and tip scans. The average reference (baseline) granite-axis temperatures were 19.3 °C and 19 °C for the base and tip scans, respectively. The average reference (baseline) steel-axis temperatures were 20.3 °C and 19.1 °C for the base and tip scans, respectively. This explains the consistent offset between the red and blue data sets  $\approx 0.3$  °C for the granite axis and  $\approx 1.1$  °C for the steel axis.

The minimum and maximum temperatures (extremes of the error bars) are used to calculate the error

in width due to the  $x$  position correction, and due to thermal strain of the  $y$ -axis. An additional  $5.5\ \mu\text{m}$  repeatability uncertainty (i.e., the length-invariant portion of the stated MicroVu accuracy) is added to the total measurement error of the petal width. This is a  $6\sigma$  repeatability bound<sup>5</sup> that is conservative for this work, and agrees well with our independent determination of repeatability errors. The resulting repeatability uncertainty in the width *change* is  $\sqrt{2} \times 5.5\ \mu\text{m}$ . With the complete post-processing method now outlined, the campaign results are presented in the following section.

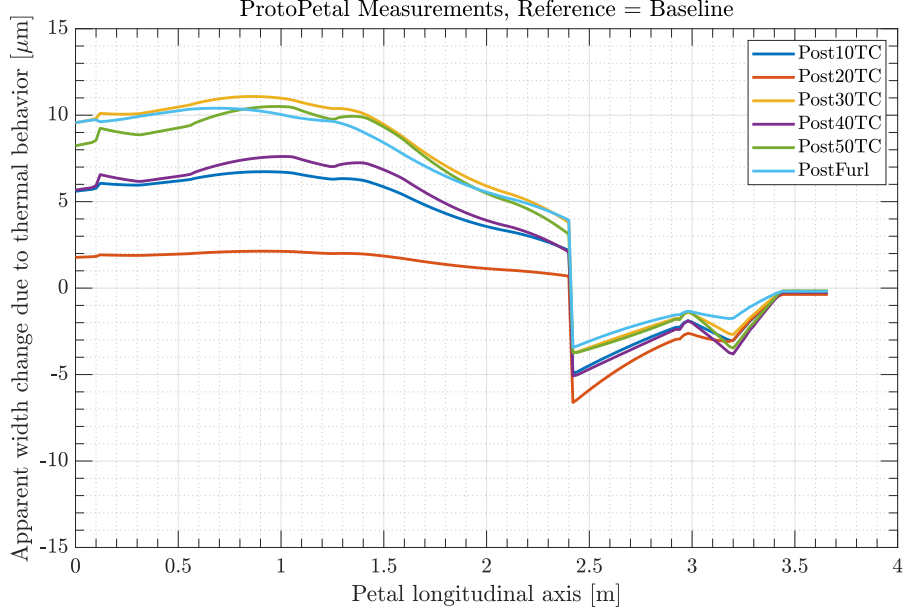
## 7 Discussion of Results

### 7.1 Corrected Data

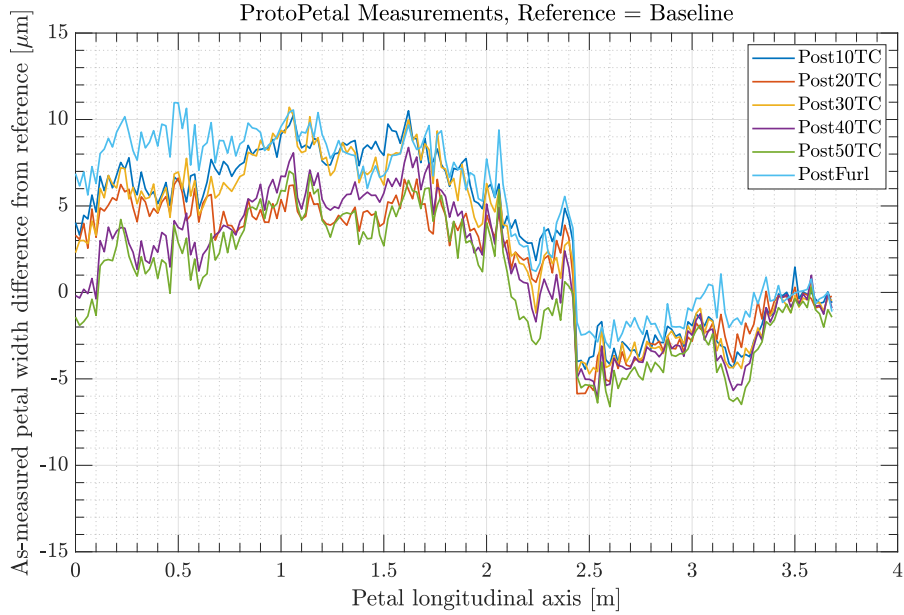
Figure 14 shows the results of the post-processing method. The sum of the error in width due to thermal strain in both the  $x$ - and  $y$ -axes corresponds to the “apparent” change in width that one would see from the MicroVu outputs solely due to differences in temperature at the time of those measurements; width error is plotted in Figure 14a for all six conditions. Figure 14b shows the as-measured (not corrected) data. The general shape signature of the measured signal corresponds well to the calculated error due to thermal strain. In particular, certain features (e.g. the one between  $x = 3$  and  $3.5\text{m}$ ) correspond extremely well to the changes in the slope of the width (Figure 12), accentuating the  $x$ -positioning error. This gives high confidence that correcting the MicroVu output data for errors due to environmental temperature differences is crucial to obtaining accurate results.

---

<sup>5</sup>From communications with MicroVu.



(a) Total width error due to thermal effects ( $x$  and  $y$ ).



(b) As-measured (not corrected) width change from the baseline for each condition.

Figure 14: Petal width errors due to thermal effects on both MicroVu axes and non-corrected (as-measured) width measurements for each condition. The error discontinuity at  $x \approx 2.4$  m is due to the use of two different sets of measurements (base and tip scans) to define the complete petal.

The corrected width changes for each condition are shown in Figure 15. The maximum uncertainty in the corrected data is illustrated with black-dashed lines, and calculated using both the uncertainty in  $\Delta T$  between the measured condition and the baseline, and the  $\pm 5.5 \mu\text{m}$  accuracy from the specification sheet. The nominal width change is contained between  $-10 \mu\text{m}$  and  $+5 \mu\text{m}$  for all conditions, and the uncertainty envelope is between  $-20 \mu\text{m}$  and  $+14 \mu\text{m}$ . The corrected petal width changes from the baseline for each measured condition are given in Appendix D. The large majority of the corrected petal width changes are

on the same order as the measurement repeatability error of the machine, i.e.,  $\pm\sqrt{2} \times 5.5 = 7.8 \mu\text{m}$ .

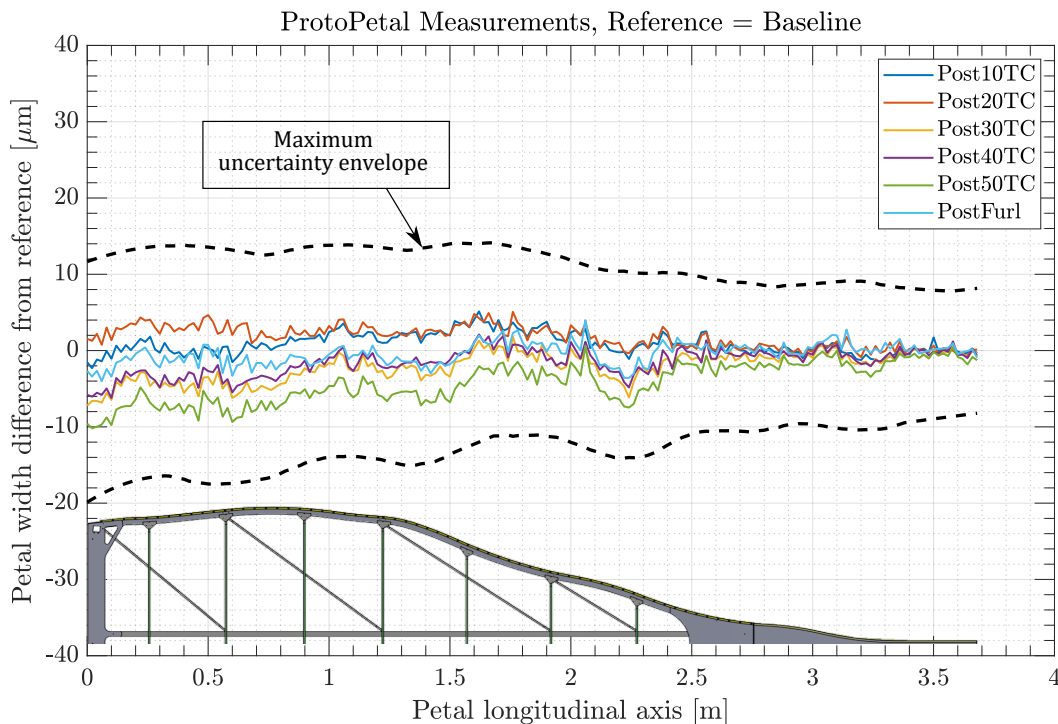


Figure 15: Corrected petal width change from baseline for each condition. The black dashed lines represent the envelope of maximum uncertainty (worst case), calculated with the uncertainty in encoder temperatures and uncertainty in width measurements.

## 7.2 Milestone Analysis

In the context of milestone 6A, a key driver of instrument contrast was determined to be the median of the width strain of the open lattice structure of the petal (e.g. portion covered by battens and braces), excluding the solid laminate CFRP tip, i.e., roughly the last meter of the petal. This metric was shown to approximate the *petal-width bias* well, and closely correlate the instrument contrast of a starshade with non-uniform petal width variations with the instrument contrast of a starshade with uniform petal width variations (Appendix C). The measured petal width strain is shown in Figure 16, including a maximum uncertainty envelope, for the portion of the petal that concerns petal-width bias. Additionally, as the petal width narrows, the uncertainty in the strain calculation increases. The nominal width strain is relatively constant from the base to the tip plate. However, because the maximum uncertainty in the petal width change is on the order of  $\pm 10 \mu\text{m}$ , the uncertainty envelope in strain grows rapidly as the petal narrows. Nevertheless, the petal-width bias using the maximum uncertainty bounds is between -12 and +10 ppm, well below the tighter global error requirement of  $\pm 24$  ppm we constrain ourselves to for milestone 5A (with the actual requirement on an individual petal being  $\pm 58$  ppm). For the environmental test considered in milestone 5A, the results allow for 100% growth<sup>6</sup> to potentially account for width variations from other sources of thermal and mechanical loads in AI&T. The petal-width bias calculated for each condition is shown in Figure 17, and the width strains with respect to the baseline for each measured condition are given in Appendix E.

<sup>6</sup>margin allowable growth is defined as  $\frac{x_{\text{requirement}} - x_{\text{measured}}}{x_{\text{measured}}}$

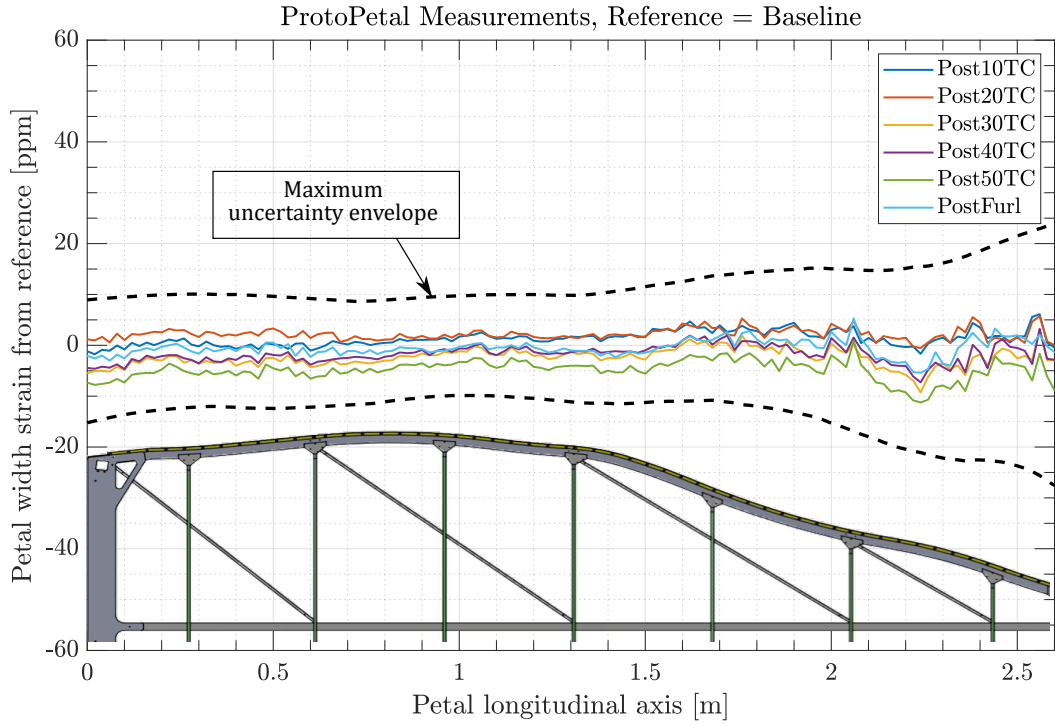


Figure 16: Petal width strain over the relevant portion of the petal for calculating petal width bias (from the base to the tip plate). The black dashed lines represent the envelope of maximum uncertainty (worst case), calculated with the uncertainty in encoder temperatures and uncertainty in width measurements.

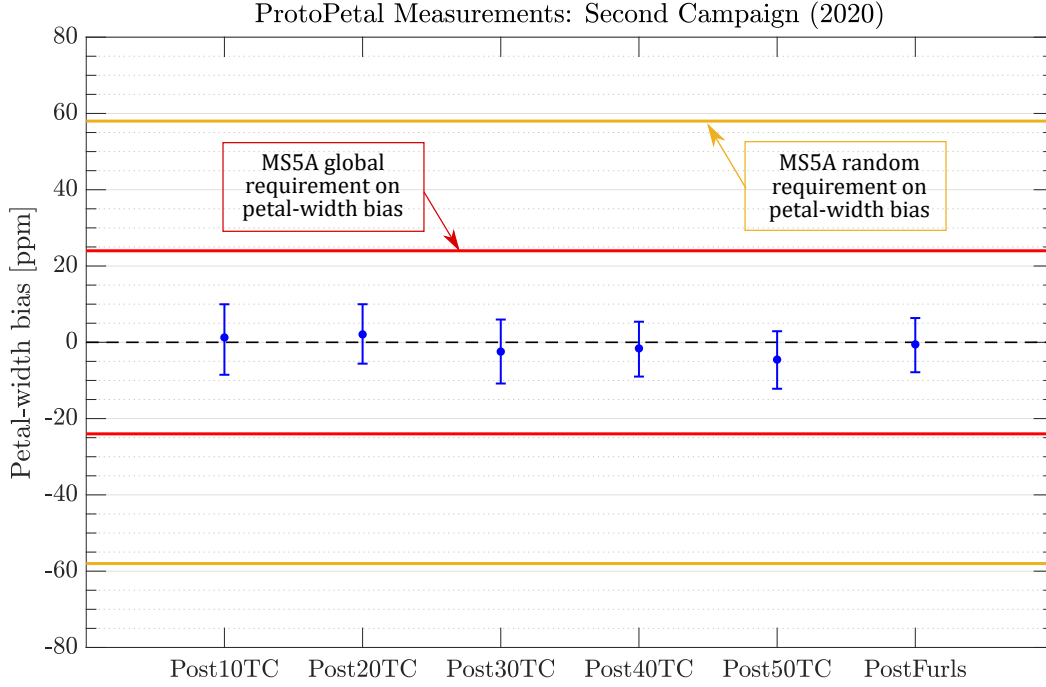


Figure 17: Petal-width bias for each condition, compared to the global error requirement of  $\pm 24$  ppm we constrain ourselves to for milestone 5A (the requirement on an individual petal being  $\pm 58$  ppm).

Since the quantity of interest is ultimately the optical performance of a starshade with an off-nominal petal shape, an optical model is used to evaluate the change in contrast due to residual shape error from thermal and deploy cycling (evaluated at a wavelength of 552 nm). This is done in two steps. First, the contrast of a starshade with a petal width strain equal to the maximum petal-width bias (-12 ppm using the uncertainty envelope) is evaluated. The resultant contrast change from nominal is  $1.5 \times 10^{-12}$  (obtained from the uniform strain curve in Figure 32). Second, the effect of the tip is evaluated by applying the strain (evaluated at maximum uncertainty) measured on the prototype petal (Figure 18) to the starshade flight petal. The computed contrast is  $1.2 \times 10^{-12}$ , ultimately an improvement from the constant strain case, even though the strains applied at the tip are on the order of  $\pm 50$ –300 ppm, orders of magnitude above the as-measured data. As a result, the change in instrument contrast assuming the worst-case measurements have been shown to be well below the milestone 5A sub-allocation of  $5.3 \times 10^{-12}$ .

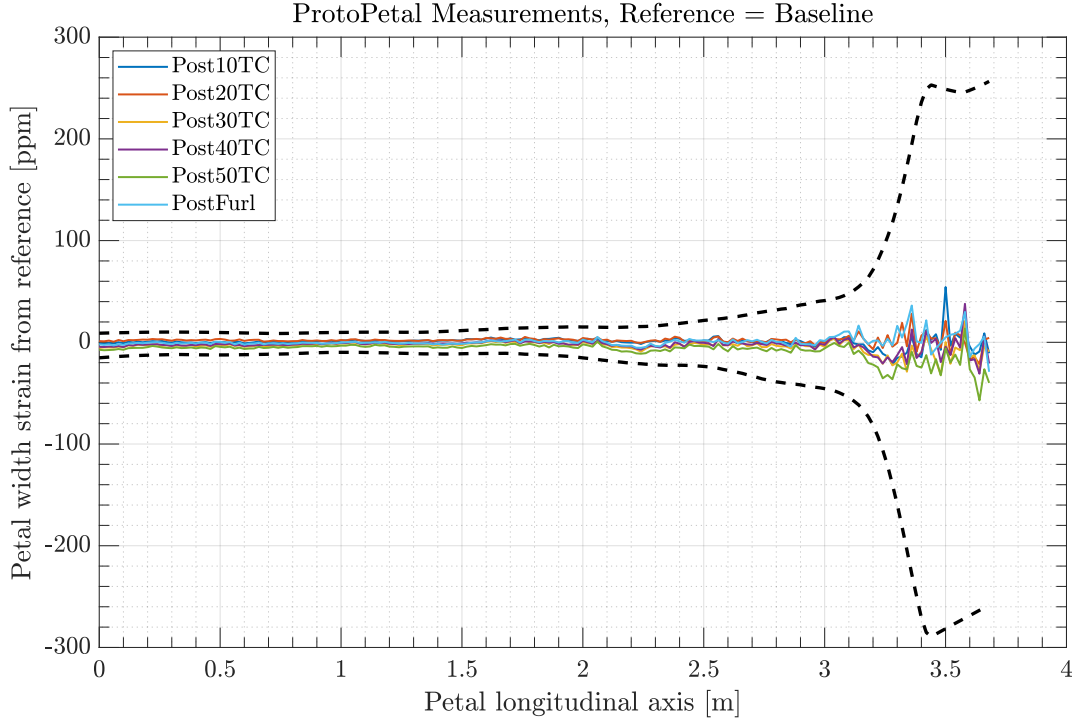


Figure 18: Petal width strain over the entire prototype petal. The black dashed lines represent the envelope of maximum uncertainty (worst case), calculated with the uncertainty in encoder temperatures and uncertainty in width measurements. The worst-case strain is applied to the starshade flight petal to determine instrument contrast change.

## 8 Conclusions

Milestone 5A requires demonstration of pre-launch shape accuracy of the petal consistent with a contribution to instrument contrast of  $1.01 \times 10^{-11}$ . To establish the shape variations after thermal and deploy cycles of a flight-like petal, a medium-fidelity prototype with shape-critical components was manufactured. The prototype petal underwent a total of 50 thermal cycles and 5 furls to the expected stowage bending radius. Throughout the process, it was measured 7 times using a microscope-based imaging device (MicroVu Excel 250ULC). The petal-width bias, i.e., the median of the petal width strain excluding the tip, has been shown to be a good parameter to characterize the optical performance of a starshade. Including conservative error estimations in the measurement post-processing, the petal-width bias across all conditions was contained between -12 and +10 ppm, allowing up to 100% growth. Furthermore, the instrument contrast change from nominal of a starshade with petal deformations equal to the worst-case measurements was evaluated at  $1.2 \times 10^{-12}$ , compared to the milestone 5A sub-allocation of  $5.3 \times 10^{-12}$ .

### 8.1 Future Work

With the completion and lessons learned from Milestone 5A, the upcoming Milestone 5B effort, which includes a medium-fidelity petal with all features, suggests four efforts near term:

- **All features:** significant work toward fleshing out the detailed design of all features, which includes understanding of the interfaces between subsystems, such that it can be evaluated again for shape accuracy after thermal and deploy cycles.
- **Moisture loss:** investigations of the uncertainty in moisture loss to understand whether it is large enough to be part of a key performance parameter for starshade on-orbit petal stability.

- **Metrology:** although the MicroVu system employed was sufficient to meet Milestone 5A, it may need upgrading or further characterization to meet in-plane shape accuracy manufacturing requirements.
- **Manufacture of a shape accurate petal with edges that meet scatter performance:** while shape accuracy has been performed with edge segments, it has not been demonstrated for edges that meet scatter performance, and represents a challenge. Milestone 5B requires the accurate placement of edges that meet scatter and in-plane shape performance.

Future programs will investigate other sources of petal shape error, including launch, deployment in space (ground to on-orbit differences), dynamics and non-quasi-static thermally induced stability errors, including ground to on-orbit changes in, and release of stored energy within the system, onboard sources of transient disturbances such as from electronics, and temporal variations of spatial temperature gradients, among others—drawing upon experiences from prior precision space optical flight systems

## Acknowledgments

This research was carried out at the Jet Propulsion Laboratory, California Institute of Technology, under a contract with the National Aeronautics and Space Administration.

## Acronyms

AI&T	Assembly, Integration, and Test
CFRP	Carbon-Fiber-Reinforced Polymer
CSZ	Cincinnati Sub Zero
CME	Coefficient of Moisture Expansion
CMM	Coordinate Measuring Machine
CTE	Coefficient of Thermal Expansion
FEM	Finite Element Method
JPL	Jet Propulsion Laboratory
KPP	Key Performance Parameter
PLUS	Petal Launch restraint and Unfurl Subsystem
ppm	parts per million
RTD	Resistance Temperature Detectors
SA	Sun Angle
S5	Starshade-to-TRL5
SRM	Starshade Rendezvous Mission
TED	Thermo-Elastic Distortion
TRL5	Technology Readiness Level 5

## References

- [1] Willems, P., “Starshade to TRL5 (S5) Technology Development Plan,” Tech. rep., Jet Propulsion Laboratory, Dec. 2018.
- [2] Kasdin, J. et al., “Advancing Technology for Starlight Suppression via an External Occulter,” Tech. rep., Jet Propulsion Laboratory, 2011, JPL Document D-68672.
- [3] Webb, D., Steeves, J., et al., “Starshade Technology Development Activity Milestone 6A Verify Petal Shape on-Orbit Stability,” Tech. rep., Jet Propulsion Laboratory, 2020.
- [4] Seager, S., Kasdin, N. J., et al., “Starshade Rendezvous Probe Study Report,” Tech. rep., Feb. 2019.
- [5] Gaudi, S., Seager, S., et al., “HabEx: Habitable Exoplanet Observatory Final Report,” Tech. rep., Aug. 2019.
- [6] Renishaw, “RGH41 RGS40 linear encoder system,” 2019.

- [7] Hockman, A. and Kessler, D. W., “Thermal and Moisture Expansion Studies of Some Domestic Granites,” *Journal of Research of the National Bureau of Standards*, Vol. 44, April 1950, pp. 395–410.
- [8] Paquin, R. A., “Materials for Optical Systems,” *Optomechanical Engineering Handbook*, edited by A. Ahmad, CRC Press LLC, 1999.

## A Thermal Response of the MicroVu Measuring Machine

As described in Section 4.3, the MicroVu measuring machine uses as length references two linear encoders, one for each axis in the measurement plane. Each linear encoder is a Renishaw RGS40 scale [6], which is a ruled gold-plated steel tape that is bonded to a substrate; along the  $x$ -axis the substrate is a granite bench, and along the  $y$ -axis the substrate is a steel bar. Variations in substrate temperature cause substrate thermal strain, which translate to thermal strain of the linear encoders. This introduces length measurement errors. The errors along the  $x$ - and  $y$ -axes are orthogonal.

To compute these errors, consider the thermal strain of the linear encoder  $\epsilon_{encoder} = \alpha\Delta T$  where  $\alpha$  is the linear encoder CTE and  $\Delta T$  is its temperature change. For a thermally invariant bar with reference length  $L_{ref}$  (defined as the measured length when the encoder thermal strain  $\epsilon_{encoder}$  is identically 0), the measured length  $L_{measured}$  at some non-zero encoder thermal strain can be computed:

$$L_{measured} = \frac{L_{ref}}{1 + \epsilon_{encoder}} \quad (3)$$

Encoder thermal strains gives rise to an *apparent* measured strain  $\epsilon_{apparent}$  of the thermally invariant bar:

$$\epsilon_{apparent} = \frac{L_{measured} - L_{ref}}{L_{ref}} \quad (4)$$

$$= \frac{-\epsilon_{encoder}}{1 + \epsilon_{encoder}} \quad (5)$$

To characterize this effect, a straightforward experiment was conducted: the temperature of the encoder substrates was varied and measured, and at each temperature, the length of a number of “truth bars” (with much lower CTE than granite or steel) was measured using the machine. From these measurements and Equation (4) and Equation (5), the apparent truth bar strain and the encoder strain at various temperatures can be calculated, thus yielding encoder CTEs.

Specifically, the “truth bars” were lengths of unidirectional pultruded CFRP (with a solid 7.94 mm-wide square cross-section) with measured CTE of  $0.13 \times 10^{-6} \text{ }^\circ\text{C}^{-1}$  in a  $17 \text{ }^\circ\text{C} \pm 10 \text{ }^\circ\text{C}$  temperature range (which encompasses the experimental conditions). Similar lengths of pultruded CFRP were used to make battens for the petal prototype. The CTE of these members was measured for Milestone 6A [3] at the Interferometric Metrology Facility at Northrop Grumman Innovation Systems.

For the present experiment, four truth bars were used, two for each axis; Figure 20 shows the location of the truth bars. The truth bars oriented along the  $x$ -axis were labeled X1 and X2, and were 1.98 m long, and the truth bars along the  $y$ -axis were labeled Y1 and Y2, and were 1.52 m long. The truth bars were elevated above the MicroVu bed, and supported in a quasi-kinematic fashion: pinned at one end, attached to a low-friction slider on the other, with two machined cylindrical rollers preventing sagging in the span while minimizing axial loads into the truth bar. The truth bars were not moved over the course of this experiment.

Optical targets were bonded to the truth bars to allow for precise length measurements. Figure 19 shows one of these targets. Each target has high-contrast features that allow for the precise measurement of the location of the center of the target using the MicroVu software. Seven equally spaced optical targets were bonded to the X1 and X2 truth bars, and six equally spaced optical targets were bonded to the Y1 and Y2 truth bars.

The temperature of the MicroVu was varied over a  $4.5 \text{ }^\circ\text{C}$  range. Four resistance temperature detectors (RTDs) were attached to the granite table to measure its temperature changes, and two RTDs were attached to the steel bar to measure its temperature changes; Figure 20 shows the location of the RTDs. The temperature of the MicroVu was adjusted by changing the room thermostat setting; the room and the MicroVu were pre-cooled to about  $16 \text{ }^\circ\text{C}$  over a weekend, the experiment began on a Monday, and the room temperature was slowly raised over the week. Table 3 shows the timeline of this experiment.

For each measurement listed in Table 3, the locations of the centers of optical targets on the truth bars were measured at the specified temperature. From this, the full length of each truth bar (i.e., the distance between the centers of the two end optical targets) can be computed. The baseline measurement was used as a reference to calculate apparent strain  $\epsilon_{apparent}$  (using Equation (4)), which was then used to calculate encoder strain  $\epsilon_{encoder}$  (using Equation (5)). The measured encoder strains are plotted against the measured changes in temperature in Figure 21. The temperature change is calculated as the mean of the changes in



Figure 19: Optical target attached to one of the truth bars.

	Timestamp (MST)	Granite temperature (°C)	Steel temperature (°C)
Baseline	2019.12.16 21:52	17.0	17.0
Measurement 1	2019.12.17 10:39	17.6	18.4
Measurement 2	2019.12.17 15:20	17.8	18.7
Measurement 3	2019.12.18 10:07	18.8	19.6
Measurement 4	2019.12.18 20:11	20.0	21.6
Measurement 5*	2019.12.19 10:19	20.5	-

Table 3: Timeline and temperatures for the MicroVu CTE measurement. \*only X1 and X2 truth bars measured.

the relevant RTD temperatures; calculating relative change in RTD temperatures prior to taking the mean removes RTD temperature bias error.

In Figure 21, the temperature error bars capture the range of  $\Delta T$  measured across the relevant RTDs, plus a random temperature error of  $0.07^\circ\text{C}$ . The strain error bars are due to MicroVu length measurement uncertainty of  $\pm 5.5\ \mu\text{m}$ ; the relationship between encoder strain uncertainty  $u(\epsilon)$  and length uncertainty  $u(L)$  was calculated to be  $u(\epsilon) = \sqrt{2}u(L)/L$ , which gives strain uncertainty of  $\pm 3.9 \times 10^{-6}$  for the longer truth bars along the  $x$ -axis, and  $\pm 5.1 \times 10^{-6}$  for the shorter truth bars along the  $y$ -axis.

For each truth bar, only the longest lengths (i.e., the distance between the centers of the two end optical targets) were used for this analysis. This is because the strain uncertainty is the smallest for the longest lengths. The shorter lengths have higher strain uncertainty and were not used for the computation of CTEs; however, strains were computed using these shorter lengths and found to be consistent with the strains measured using the longest lengths.

Error in calculated encoder strain due to treating the truth bars as being invariant in length (i.e., with 0 CTE) when in reality they have some small CTE ( $0.13 \times 10^{-6} \text{ }^\circ\text{C}^{-1}$ ) is less than 3% for the  $x$ -axis, and less than 2% for the  $y$ -axis. Error in calculated encoder strain due to angular misalignment between the truth bars and the machine axes (which was measured to be less than  $0.5^\circ$ ) is less than 0.003%.

As can be seen from Figure 21, the relationship between encoder thermal strain and delta temperature is linear. The slopes of the linear fits yield encoder CTEs:  $4.9 \times 10^{-6} \text{ }^\circ\text{C}^{-1}$  for the  $x$ -axis encoder affixed to the granite bench, and  $11.2 \times 10^{-6} \text{ }^\circ\text{C}^{-1}$  for the  $y$ -axis encoder affixed to the steel bar. (Standard errors on the coefficients of the linear fits are  $0.1 \times 10^{-6} \text{ }^\circ\text{C}^{-1}$  for the  $x$ -axis and  $0.3 \times 10^{-6} \text{ }^\circ\text{C}^{-1}$  for the  $y$ -axis.) These

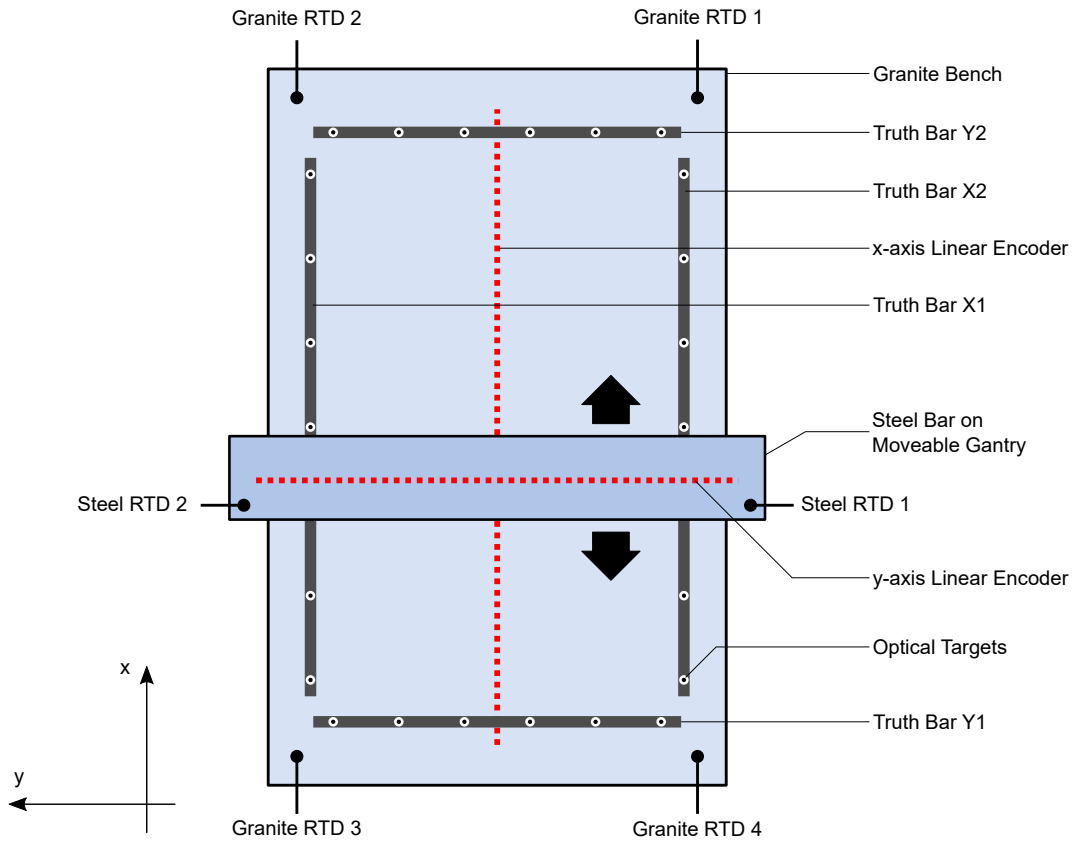
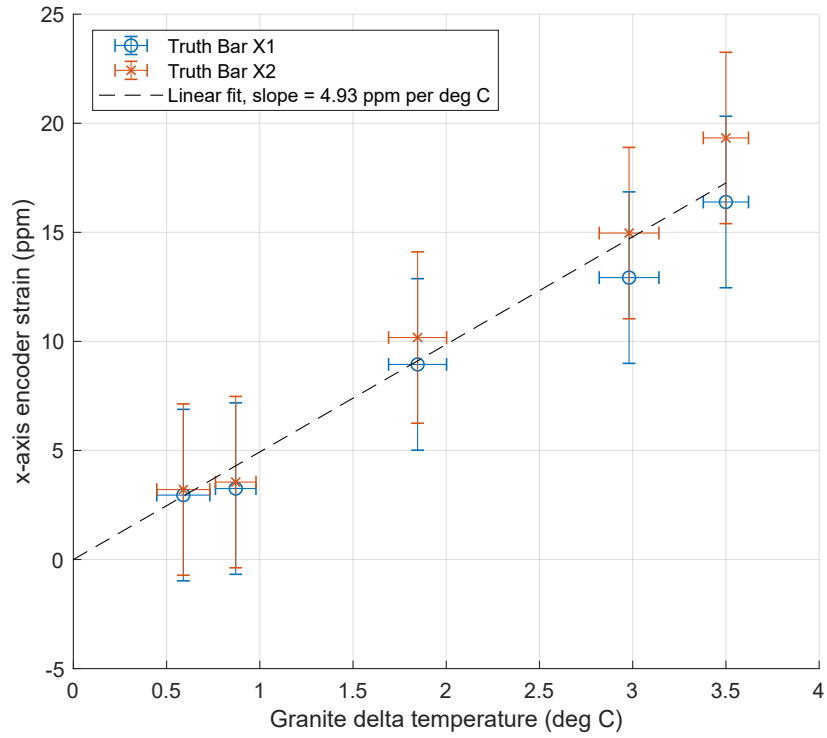
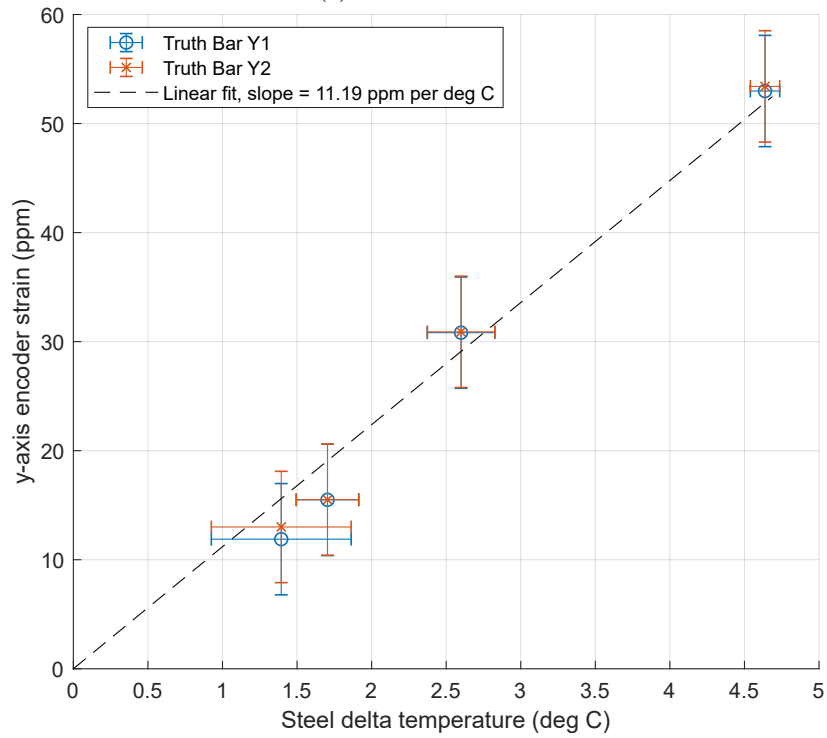


Figure 20: Schematic of the MicroVu instrumented for CTE measurement of the two linear encoders.

values compare well to accepted CTE values of the substrate materials to which the corresponding linear encoders are mounted: granite for the  $x$ -axis (reported CTE between  $4.8 \times 10^{-6} \text{ }^\circ\text{C}^{-1}$  and  $8.3 \times 10^{-6} \text{ }^\circ\text{C}^{-1}$  [7]) and steel for the  $y$ -axis (reported CTE between  $8.5 \times 10^{-6} \text{ }^\circ\text{C}^{-1}$  and  $14.7 \times 10^{-6} \text{ }^\circ\text{C}^{-1}$  [8]).



(a) *x*-axis encoder.



(b) *y*-axis encoder.

Figure 21: Measured CTE of the MicroVu encoders.

## B First Environmental Testing Campaign

This appendix presents the data collected during a first measurement campaign carried out at the Tendeg facility in Louisville, Colorado between March and September 2019. Temperature effects on the MicroVu measurements were not taken into account during this campaign and the results showed unrealistically large shape changes (up to 50  $\mu\text{m}$  changes in petal width), which are larger than the thermal deformations measured during the temperature excursions in milestone 6A. To compare the initial as-manufactured petal shape to the shape after the first set of environmental testing, effort was put towards determining the machine temperatures to correct the data.

### B.1 Experimental Approach

The total number of thermal cycles in the first campaign was 16, distributed in four series of 1, 4, 5, and 6 cycles. The petal was removed from the chamber and placed on the MicroVu for measurement between each series. The last set of 6 cycles were performed for the purpose of the thermo-elastic distortion (TED) testing for milestone 6A, and were therefore not continuous like the previous series. However, the petal was not removed from the chamber during this time. Following thermal cycling, the petal was installed on the furling fixture, which enforced the flight furling radius once. It was remeasured and then furled 4 more times before the final measurement. The complete set of data for this first campaign therefore includes 7 different conditions, listed in table Table 4 with the respective measurement dates.

Measurement date	Condition	Data reference name
2019.03.29	Baseline	Baseline
2019.04.03	1 thermal cycle complete	Post1TC
2019.04.08	5 thermal cycles complete	Post5TC
2019.04.25	10 thermal cycles complete	Post10TC
2019.08.12	16 thermal cycles complete	Post16TC
2019.08.20	1 deploy cycle complete	Post1Furl
2019.09.23	5 deploy cycles complete	Post5Furls

Table 4: Petal testing and measurement timeline for the first environmental campaign.

The measurement method on the MicroVu differed from the second environmental campaign in that only point measurements were recorded on each edge, as opposed to the 1 mm-wide windows. To define the complete petal shape, 77 points are taken from a base scan and 40 points from a tip scan, totalling in 117 points spaced roughly 3.2 cm apart. The local coordinate system was defined in the same way, using the 4 optical targets bonded to battens numbered 4 through 7 from the root. The single-point output complicates the data-correction process in that the shape of edge needs to be inferred to account for  $x$  positioning error. The  $y$  coordinate of the edge at a corrected  $x$  location is therefore calculated using cubic spline interpolation.

### B.2 As-measured Data

The petal width is derived from measuring the  $y$  distance between two points on opposing edges. To account for errors in alignment from one edge to another, reference  $x$  coordinates are defined from the first edge of the baseline scan. All of the points on the second edge of the baseline scan are computed by interpolating between the acquired data points. The calculated widths are therefore all parallel to each other and perpendicular to the local longitudinal axis of the petal defined by the optical targets on battens 4, 5, 6, and 7. The petal width changes from the baseline for the 6 different conditions are shown in Figure 22.

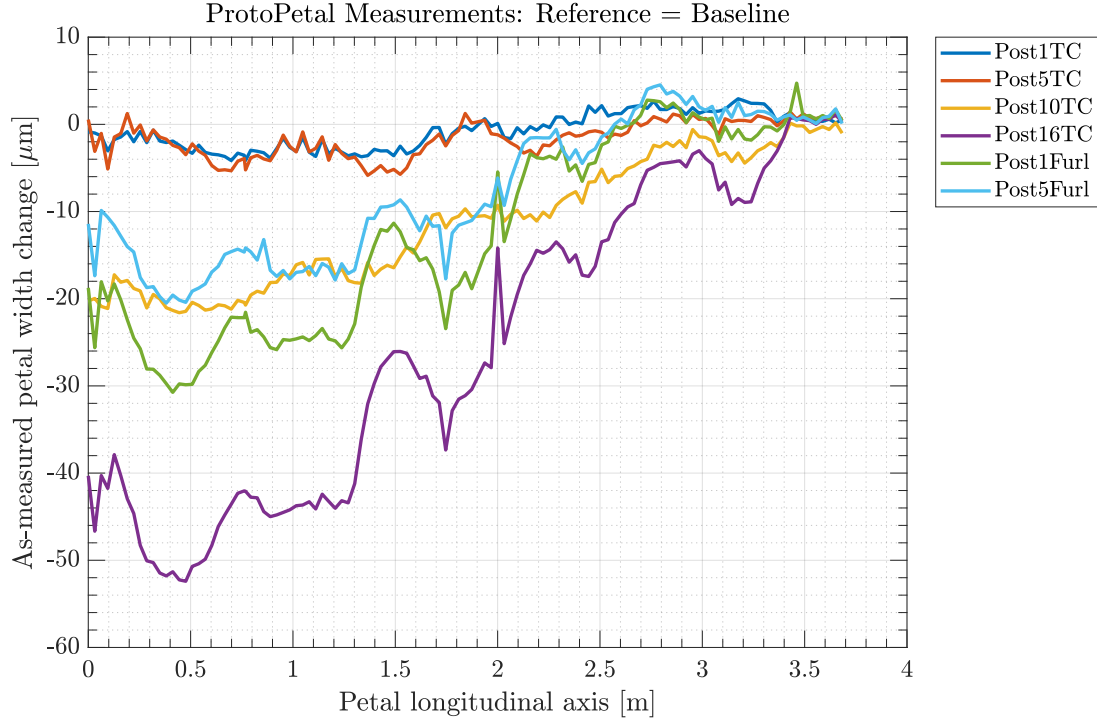


Figure 22: Width change from baseline for each condition. The data is corrected to calculate petal widths at reference  $x$  locations defined from the first edge of the baseline scan.

### B.3 Temperature Correction

The challenge with this first campaign is the lack of direct temperature data of the machine encoders. The temperature difference from the baseline ( $\Delta T$ ) is necessary to correct for the metrology machine’s thermal behavior. Nevertheless, to infer the temperature from the acquired data in the first campaign, two different approaches were taken. The first evaluates the  $\Delta T$  that minimizes the mean residual of the corrected width change. The second uses the displacements measured in the optical targets located on the battens, braces, and spine of the petal.

For the first approach, a range of  $\Delta T$  between  $-1^\circ\text{C}$  and  $4^\circ\text{C}$  are used to evaluate the petal width after correcting for thermal errors on the both the  $x$ - and  $y$ -axes; refer to Section 6 for more details on the correction process. This method assumes the temperature of both axes are equal. The  $\Delta T$  that minimizes the mean corrected petal width change is then used as the temperature offset from baseline for the measurement of a given condition. The total width error due to thermal effects in  $x$  and  $y$  using this  $\Delta T$  result is shown in Figure 23 for all conditions. This corresponds to the “apparent” change in width that one would see from the MicroVu outputs solely due to differences in temperature at the time of those measurements. The shape signature of the as-measured data (Figure 22) corresponds well to this calculated error due to thermal strain (Figure 23).

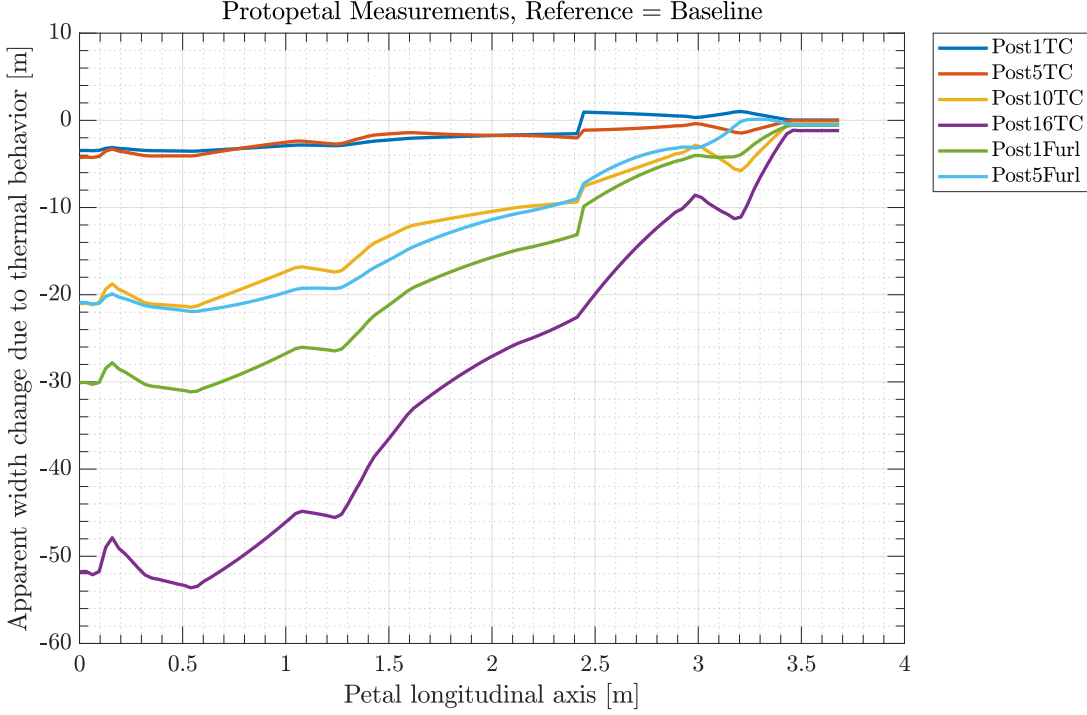
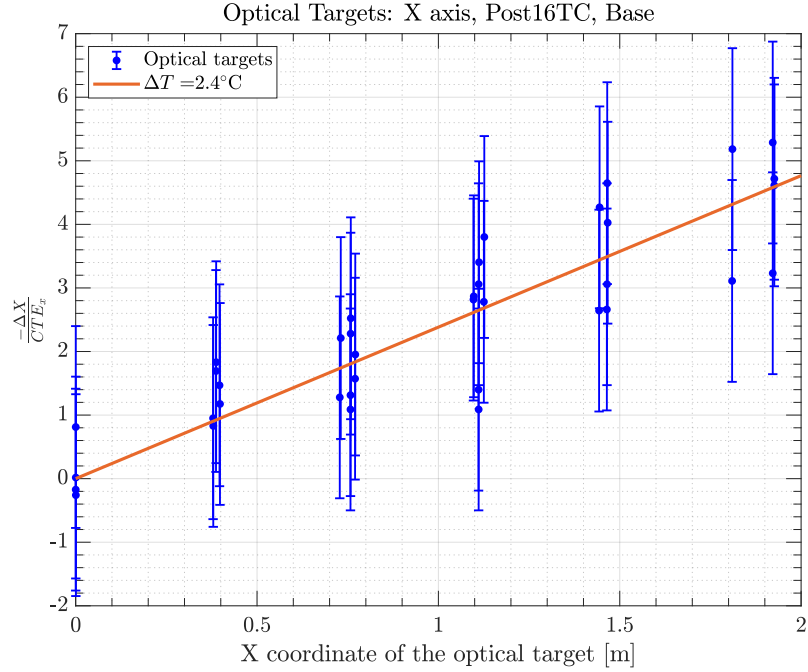


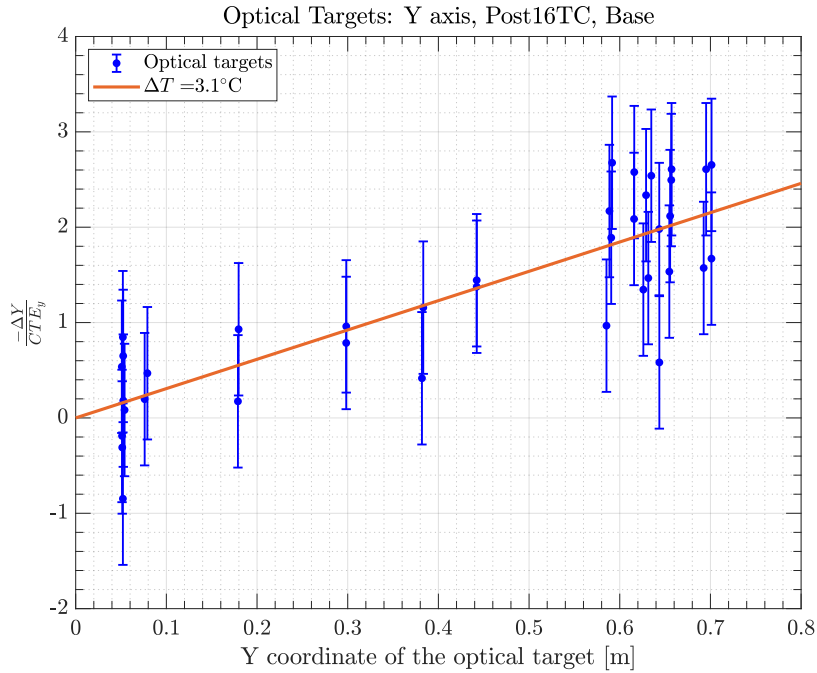
Figure 23: Total width error due to thermal effects on  $x$ - and  $y$ -axes of the MicroVu. The  $\Delta T$  from baseline is inferred from the value that minimizes the residual of the corrected width change. The discontinuity at  $x = 2.4\text{m}$  is due to the separate base and tip scans to define the complete petal width.

The second approach uses optical targets (3.3 mm circles with crosshairs) bonded to the battens, braces, and spine of the petal. 38 optical targets are captured on the base scan, and 21 targets are measured on the tip scan. The advantage of using the optical targets is that they provide more repeatable measurements than the edge. The MicroVu is commanded to search for an optical target around a hard-coded location, but will search and find the feature anywhere on the microscopy image. Conversely, when measuring a point on the terminal edge, there is no marker for the microscope to look for, so the output can be points at different  $x$  locations. The optical targets are therefore used in a similar fashion as the truth bars in Appendix A, except that the unknown in this problem is the temperature difference from the baseline  $\Delta T$ , which is the slope of the linear function relating the change in target position from the baseline  $\Delta X = X_{measured} - X_{ref}$  to the target position  $X_{measured}$ , given in Equation (6). The same process is used for the coordinates along the  $y$ -axis. Results are shown for both  $x$ - and  $y$ -axes for the PostTC16 condition in Figure 24. This method assumes that the displacements of the optical targets are solely due to machine thermal strain.

$$\begin{cases} X_{ref} = X_{measured}(1 + CTE_x \Delta T) \\ \frac{-\Delta X}{CTE_x} = \Delta T \times X_{measured} \end{cases} \quad (6)$$



(a) Optical target displacements in  $x$ .



(b) Optical target displacements in  $y$ .

Figure 24: Optical target displacements in  $x$  and  $y$  for Post16TC. The slope of the curve corresponds to the difference in temperature from the baseline, according to the thermal characterization of the MicroVu. The uncertainty in  $\Delta X$  and  $\Delta Y$  is calculated from the machine uncertainty of  $5.5 \mu\text{m}$  and is equal to  $\sqrt{2} \times 5.5 = 7.8 \mu\text{m}$ .

The temperature offsets obtained with the second method are in good agreement with the results from

the first method, and summarized in Table 5 for the base scans and Table 6 for the tip scans. The results for the tip scans do not agree as well as for the base scans because the measured part lengths are relatively small.

Condition	Optical targets		Corrected petal width
	$\Delta T_x$	$\Delta T_y$	$\Delta T$
Post1TC	0.2	0.2	0.2
Post5TC	0.5	0.2	0.2
Post10TC	1.3	1.2	1.2
Post16TC	2.4	3.1	2.7
Post1Furl	1.4	1.8	1.4
Post5Furls	0.7	1.3	1

Table 5: Base scans: inferred temperature differences from the baseline using two different methods: minimization of the residuals of the corrected petal width, and optical target displacements. All numerical values are expressed in degrees Celsius.

Condition	Optical targets		Corrected petal width
	$\Delta T_x$	$\Delta T_y$	$\Delta T$
Post1TC	-0.2	-0.1	-0.4
Post5TC	0.3	0.1	-0.1
Post10TC	1	1	0.8
Post16TC	1.5	3.3	1.5
Post1Furl	0.4	1.6	0
Post5Furls	-0.4	1.4	-0.3

Table 6: Tip scans: inferred temperature differences from the baseline using two different methods: minimization of the residuals of the corrected petal width, and optical target displacements. All numerical values are expressed in degrees Celsius.

## B.4 Discussion of Results

The petal width data was corrected using the temperature differences derived from both methods described in the previous section, and the the resulting width strain for one set of  $\Delta T$  values is shown in Figure 25.

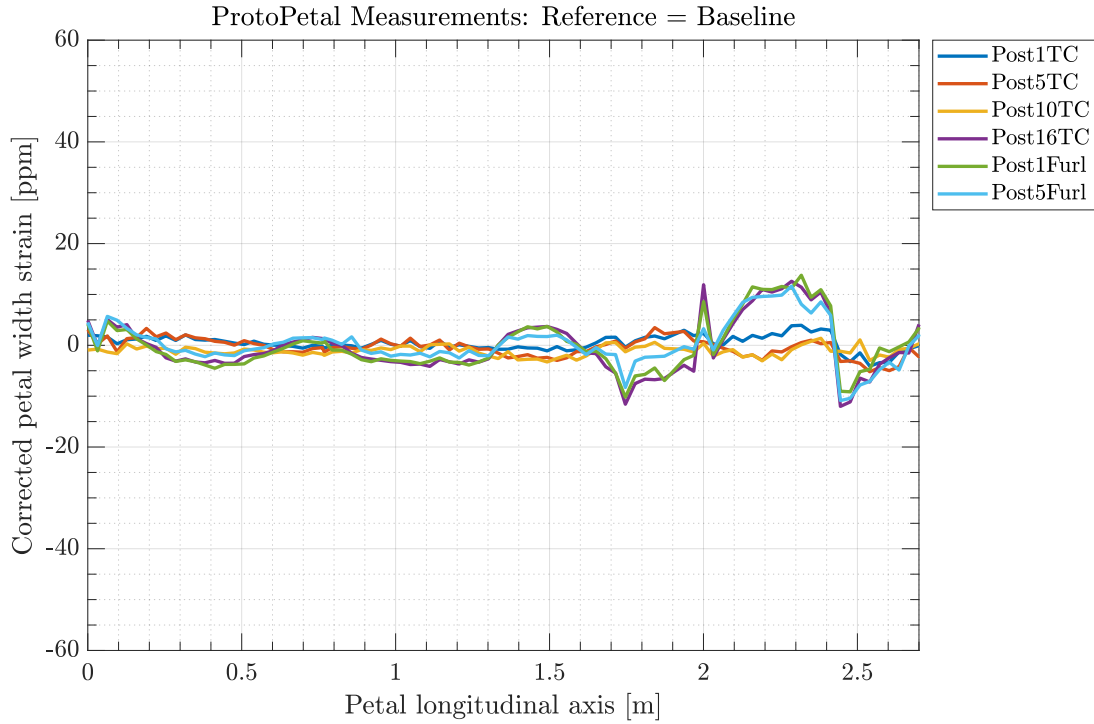


Figure 25: Corrected petal width strain for each condition assuming an average  $\Delta T$  derived to minimize the residual width change. The data is shown over the portion of interest of the petal used to calculate the petal-width bias, from the base to the tip plate.

The petal-width bias is derived for the temperature-corrected strain using the two different  $\Delta T$  calculation methods for all conditions, shown in Figure 26. The error bars are computed assuming a temperature uncertainty of  $\pm 0.3^\circ\text{C}$  (average error in  $\Delta T$  between the two methods for the base scans) and a machine error of  $5.5\ \mu\text{m}$ .

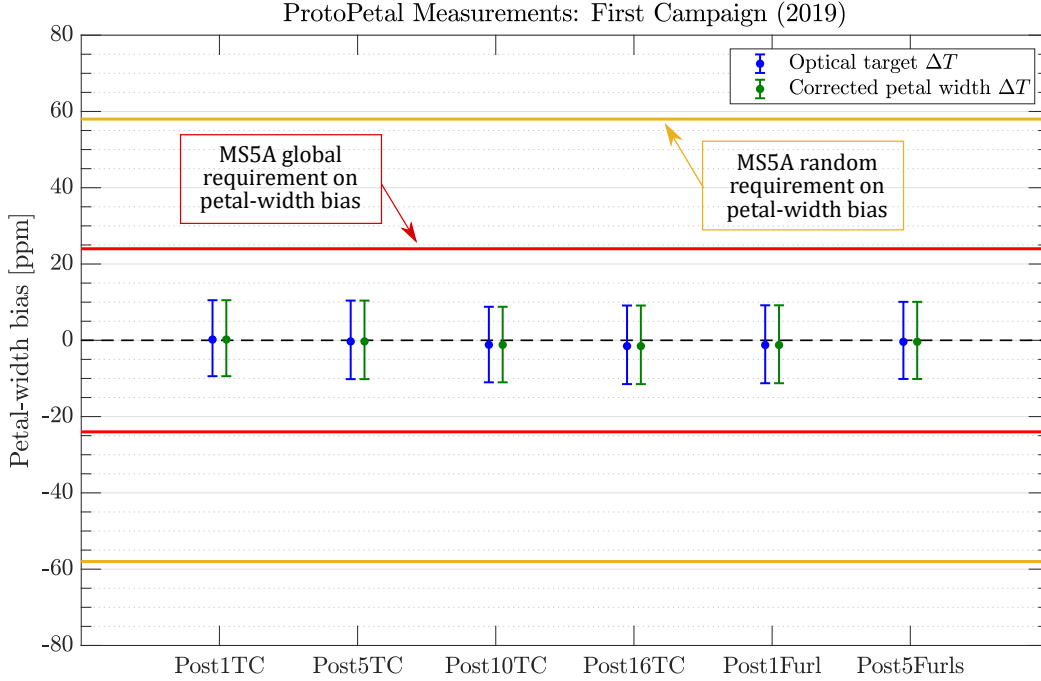


Figure 26: Petal-width bias for each condition, compared to the  $\pm 24$  ppm global requirement established for milestone 5A (in red) and the  $\pm 58$  ppm random requirement (in yellow). Uncertainty bounds are calculated for a temperature uncertainty of  $\pm 0.3$  °C.

## B.5 Summary

The limitations of this analysis rely on the lack of direct temperature data on both axes of the MicroVu, and on the cubic spline interpolation between sparse petal data. Additionally, the MicroVu measurement script did not guarantee output images that were consistently in focus, introducing a large source of error when determining single point measurements along the edge. All of these limitations were mitigated for the second environmental testing campaign. New measurement scripts were written to ensure optimal focus and lighting and capture a window of edge instead of a single point for more accurate temperature corrections using real-time RTD measurements.

Nevertheless, the as-measured petal width change has a general shape signature that corresponds well to the thermal behavior of the metrology machine, and from which the temperature difference from the baseline can be inferred. As an additional verification approach, the  $\Delta T$  was also computed using optical targets bonded to the petal and used as “truth” measurements. The results were very consistent between the two methods, with a maximum difference (for the base scans) of  $\pm 0.4$  °C. The nominal results for petal-width bias were all between  $-2$  and  $+5$  ppm, strongly suggesting that the majority of the actual petal width changes were below the measurement capabilities of the MicroVu machine. Computing uncertainty bounds on this data is not a trivial process, and a more conservative approach could be used. Nevertheless, assuming a  $\Delta T$  uncertainty of  $\pm 0.3$  °C, the worst-case petal-width bias across all conditions is evaluated between  $-12$  and  $+14$  ppm, allowing for 71% growth against the available headroom (not including other error sources).

## C Petal-width Bias<sup>7</sup>

This Appendix details the definition of the *petal-width bias* that was adopted to characterize the key performance parameter defining petal on-orbit shape stability, the driver of on-orbit instrument contrast. This metric aims to accurately predict change in instrument contrast for a given thermally deformed petal. The reference curve is the change in instrument contrast for a perfect petal-width bias, which has uniform petal-width strain. We look for correlation between our petal-width bias metric for the actual thermally deformed petals, and that reference curve. We determined that an accurate metric of petal-width bias is the median of the thermal width strain, excluding the petal tip. This metric was defined by analyzing various thermally deformed petals for the validated flight-design, as well as numerically created shapes applied to the flight design (with no actual physical effects driving strain). This metric was validated against our reference curve. The difference between the validated Finite Element Model (FEM) and simulated cases, and the reference curve, is the uncertainty in the prediction. This difference is shown to be due to variations in the thermal strain around the petal-width bias, particularly at the petal midspan locations, and the tip. Nevertheless, over all the simulated cases spanning the range of expected thermal deformations, the deviation from the uniform strain curve was less than 1.2 ppm. Therefore, we can compute the petal-width bias utilizing the median of the thermal width strain, excluding the petal tip, and our calculation of petal-width bias will be accurate within  $\pm 1.2$  ppm. We apply this petal-width bias uncertainty against the requirement in quadrature with our measurement uncertainty in our milestone analysis.

### Key Components of the Petal

In the following sections,  $x$  refers to the longitudinal axis of the petal, and  $y$  the width-wise axis of the petal. As described in section 3.1, critical features that define the petal include the intersection of the batten with the optical edge, and the points on the edge between two battens, referred to as the midspans. The thermally induced deformations are relatively uniform at the petal edges corresponding to the batten-rod  $x$  locations, since these members are stiff, with minor variations in CTE (section 2.4). However, the optical edge displacements at the more compliant midspan locations are also affected by the movement in both  $x$  and  $y$  of the neighboring battens, and present much larger variations. The tip plate is made of quasi-isotropic CFRP, which has a CTE of roughly 0.0055 ppm/ $^{\circ}\text{C}$  at  $-50^{\circ}\text{C}$ , in the width-wise direction. But as the petal width gets thinner—by a factor of 7.5 with respect to the widest part of the tip plate—the CTE of the adhesive (EA9394, 63 ppm at  $-50^{\circ}\text{C}$ ) has a larger contribution to the width-wise thermal behavior. This results in very large strains at the tip, up to 25 times the thermal strain evaluated at the battens. These critical features are shown in Figure 27, and are used in the following simulations to define modified petal deformations and evaluate the effect of petal shape stability on optical contrast.

---

<sup>7</sup>The content of this section has already been described in the Starshade Technology Development Activity Milestone 6A Report, and is repeated here for clarity. Some of the analysis was specifically catered toward on-orbit thermal deformations but was maintained here for consistency. The work is still consistent for milestone 5A in that it supports the use of the petal-width bias term as a metric to characterize on-orbit instrument contrast.

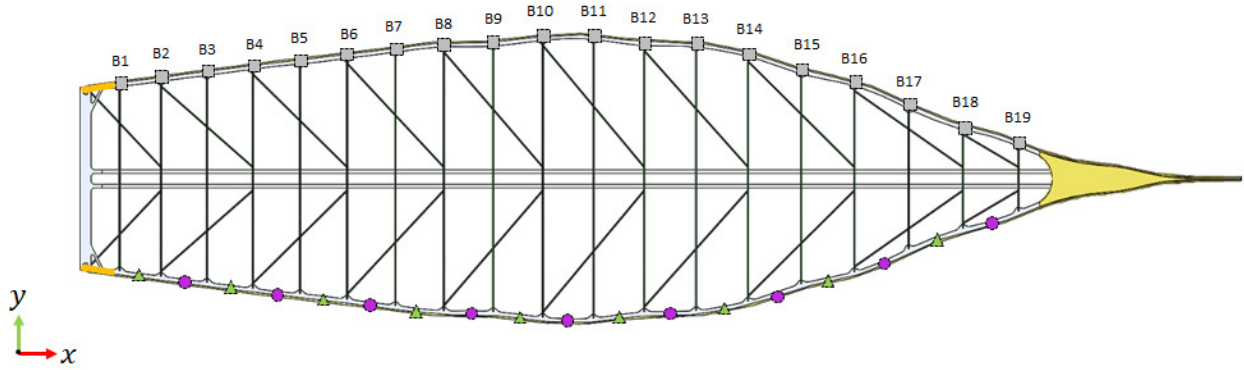


Figure 27: Flight-design petal with critical features highlighted. The 19 intersections of the battens with the optical edge (numbered gray squares on the top edge) are the most deterministic locations. The midspans (shown on the lower edge) are divided into two groups referred to as “odd” (green triangles) and “even” (magenta circles), and are differentiated by the location of the diagonal brace. The width-wise strain at the root and at the tip plate, shown in yellow, are also factors in determining the overall shape of the optical edge.

## Petal Shape Variations

To evaluate the effect of petal-width variations on the optical performance of the starshade, and extract a correlation factor defined as the *petal-width bias*, different petal shapes were created with either thermal FEM predictions, exaggerations of those predictions, or artificially imposed variations. The analysis of the artificial variations was used to validate the definition of the petalwidth bias (defined as the median excluding the tip) and obtain a sample set spanning the expected range of variations. To artificially modify the shape of the petal from the nominal flight design, strains were imposed on a number of control points at the root of the petal, the batten locations, the midspan locations, and the tip plate (Figure 6-1). The strains at the remaining points that define the optical edge were calculated by cubic spline interpolation, using the previously defined control points as queries. The word “artificially” is used here to differentiate these cases from those where the petal widths were obtained directly with the results of the flight-design, validated FEM. Three different series of cases (A, B, and C) are described below:

- A. **Constant width strain imposed everywhere along the petal.** These cases are equivalent to assuming that the petal is constructed of a single material of uniform CTE, and undergoes uniform thermal soak. The petal grows or shrinks with a constant width-wise strain from the root to the tip.
- B. **Artificial width strain imposed using regular patterns.** A constant width strain ( $\pm 10$ ,  $\pm 20$ , or  $\pm 25$  ppm) is imposed at the 19 batten locations, between the root and the first batten, and at the tip plate. Additionally, variations between the battens are introduced by forcing the strain at the midspan locations to a constant value (within  $\pm 25$  ppm of the battens). The midspans either all have the same strain (all the same direction), or are set so that the even and odd midspan strains alternate around the batten strain (Figure 28 and Figure 29).

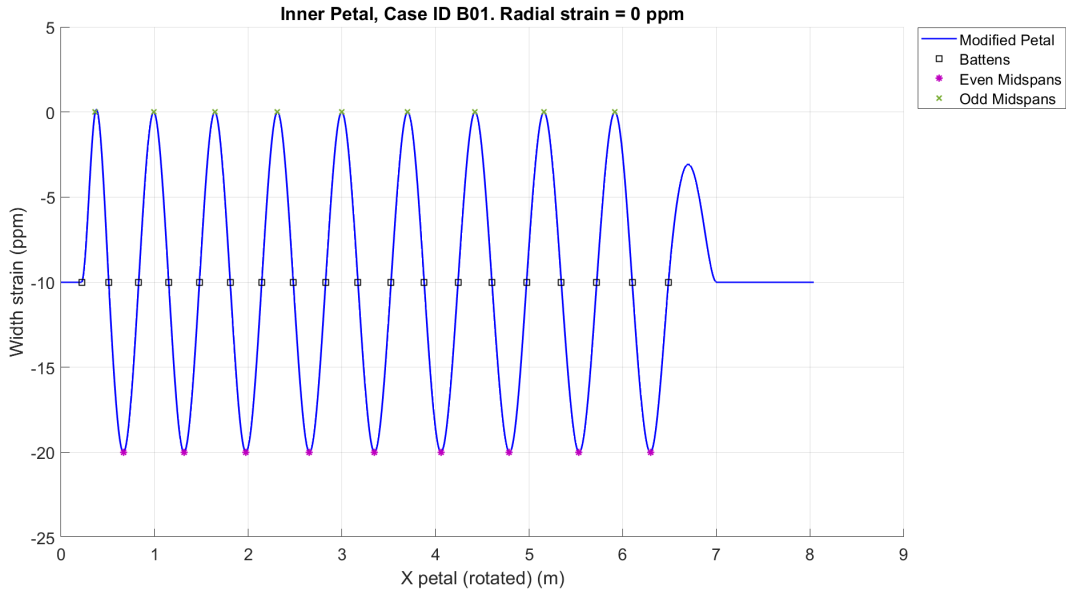


Figure 28: Artificially imposed width strain along the petal length. For B01, the root, battens, and tip are set to -10 ppm, all even midspans set to -20 ppm, and all odd midspans set to 0 ppm, creating an alternating pattern.

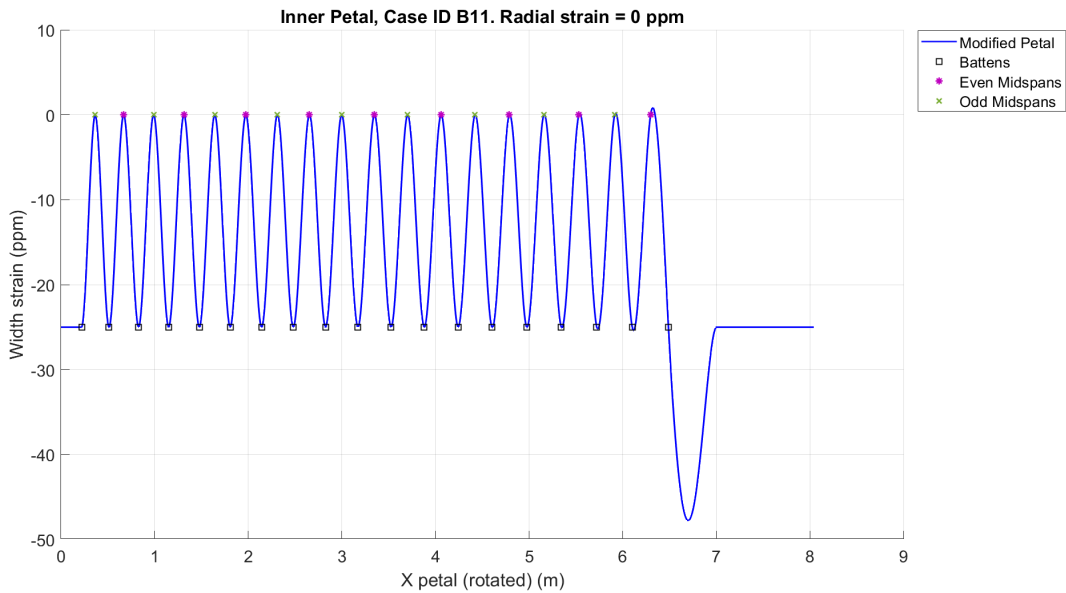


Figure 29: Artificially imposed width strain along the petal length. For B11, the root, battens, and tip are set to -25 ppm, and all even and odd midspans set to 0 ppm.

**C. Width strain imposed used flight-design, validated FEM outputs.** Various simulations, including the worst-case conditions, were analyzed to evaluate the petal shape stability at different sun angles, and were presented in this report. The change in instrument contrast of starshades with these petal-width distributions is evaluated and compared to the metric defined as petal-width bias. These cases include results for sun angles of  $83^\circ$  or  $40^\circ$  (SA83 and SA40, respectively), with the worst-case

condition ( $3\sigma$  CTEs & temperature uncertainties of  $\pm 10^\circ\text{C}$ ), and also, scenarios with very large CTE variations, e.g. up to 100% increase (which is an arbitrary variation value). Petal-width strain as a function of  $x$  is shown in Figure 30 and Figure 31 for SA40 and SA83.

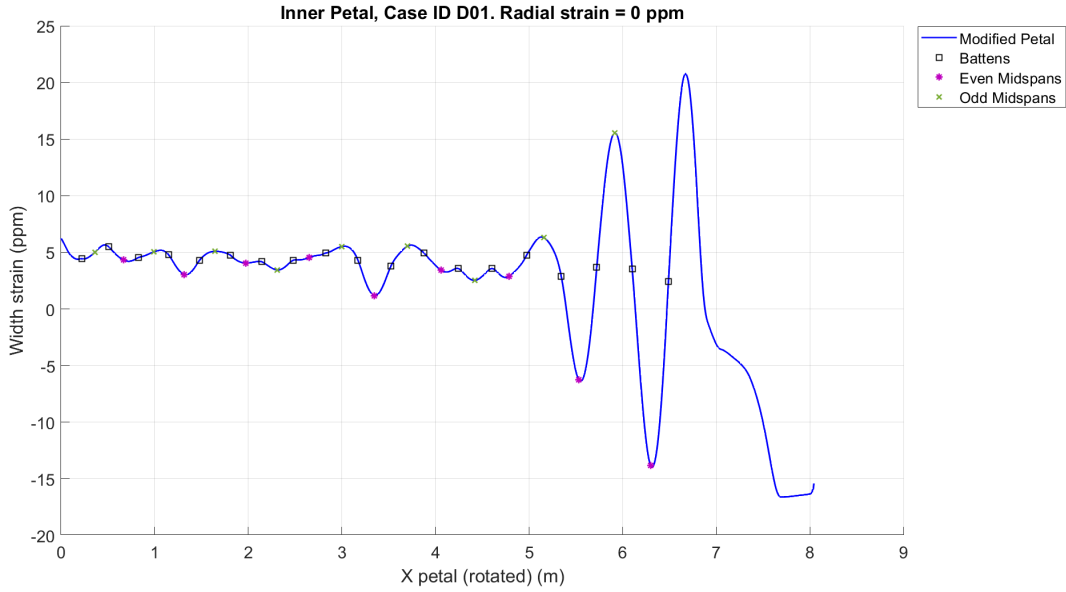


Figure 30: Flight-design validated FEM results for the width strain along the petal length for a sun angle of  $40^\circ$  (hot).

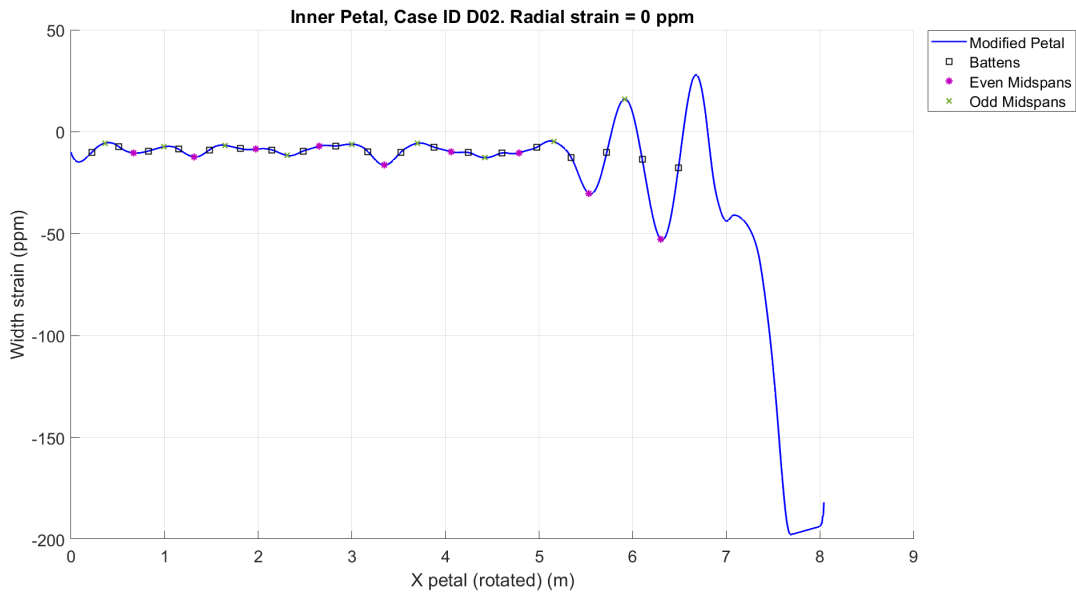


Figure 31: Flight-design validated FEM results for the width strain along the petal length for a sun angle of  $83^\circ$  (cold).

## Correlation Between Instrument Contrast and Petal-width Bias

Analysis of the change in instrument contrast of starshades with petal widths modified from nominal (following the process described in the previous section), showed that the instrument contrast was proportional (in quadrature) to an overall change in petal width-wise strain. More specifically, large variations at the midspans did not have a strong effect on contrast, and the driving parameter could be defined as the median of the width strain, calculated from the root of the petal to the beginning of the tip plate ( $x \approx 7\text{ m}$ ), excluding any contributions from the tip. Although the average of the petal-width strain was considered as a metric, it was too sensitive to variations in the midspans. The median, however, is not skewed by small proportions of extremely large or small values, and characterizes the strain at the midpoint of the distribution. The following results show the strong correlation between this term and the change in instrument contrast for a wide range of petal shapes. As a result, the petal-width bias is simply the median of the petal-width strain, excluding the tip plate.

- A. **Constant width strain imposed everywhere along the petal.** These results serve as the optical performance reference, with the contrast change from nominal following a quadratic behavior as a function of the petal-width bias, as expected (Figure 32).

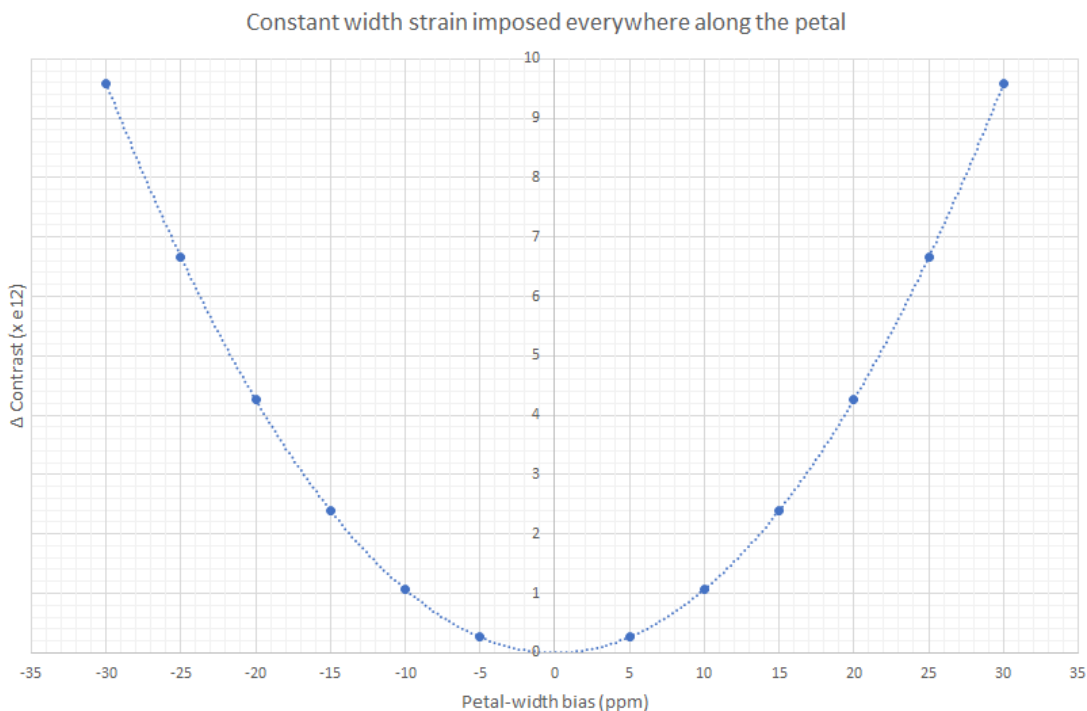


Figure 32: Contrast difference between starshades with petals with constant width strain and the nominal design.

- B. **Artificial width strain imposed using regular patterns.** Although the variations in strain of the midspans were quite large in some of these cases (up to  $\pm 25$  ppm), the petal with regular strain patterns imposed, when evaluated at the petal-width bias, followed the reference curve with strong correlation (Figure 33). The correlation uncertainty, defined as the strain difference between the measured petal-width bias and the petal-width bias of the reference curve, was below 1.7 ppm.

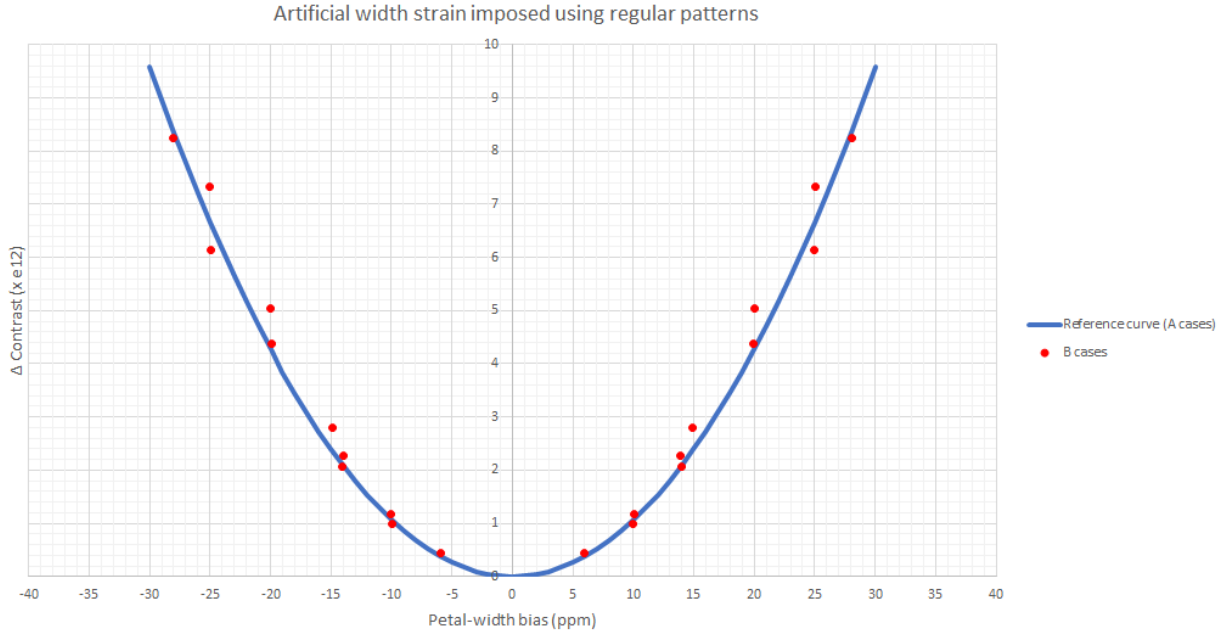


Figure 33: Contrast difference from nominal for starshades with petals undergoing artificial variations, with constant strains imposed at the root, battens, tip, and midspans (red points). The reference curve (constant strain cases A) is added for reference, and demonstrates a strong correlation as a function of petal-width bias (median up to 7 m).

- C. **Width strain imposed used flight-design, validated FEM outputs.** The contrast difference from nominal of starshades with petal widths predicted by the FEM also followed the reference curve when using the petal-width bias as a characteristic metric of shape change (Figure 34). It is important to note that these thermally deformed petals are for the on-orbit predicted temperatures, but they are maintained at the nominal (non-deformed) disk radius. This results in a net larger change in contrast for the given thermally deformed petal. This logically follows because the petal-width bias error will be larger for the cases presented herein, as compared to ideal disk radius. The correlation uncertainty was below 1.2 ppm for the cases of interest to our on-orbit scenarios.

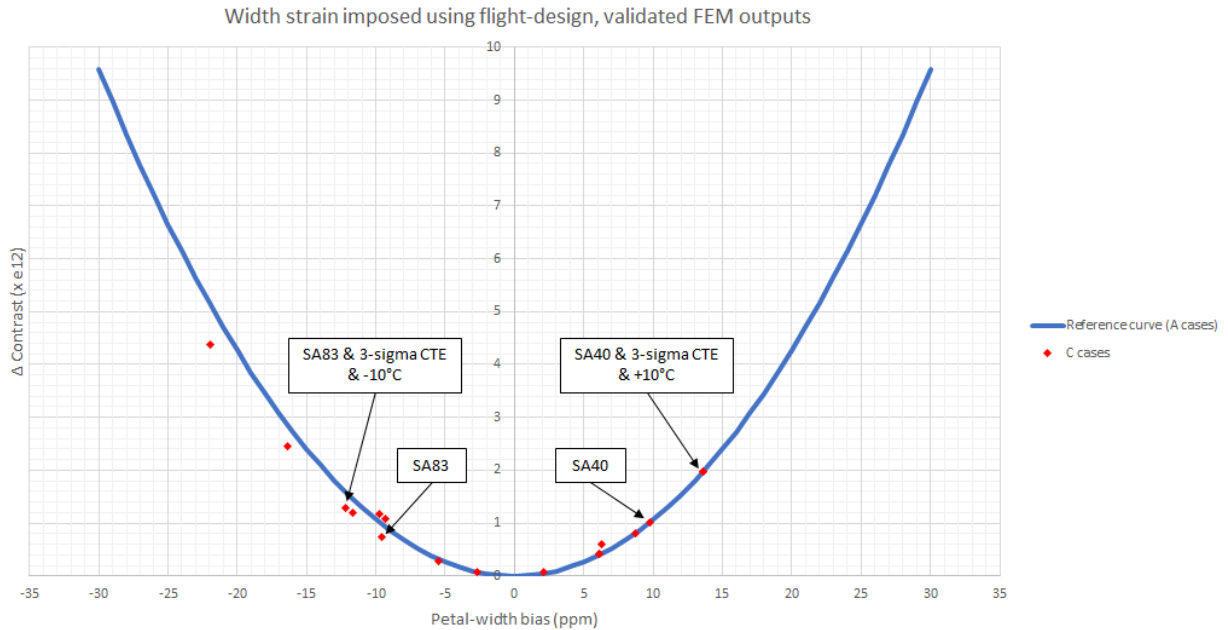
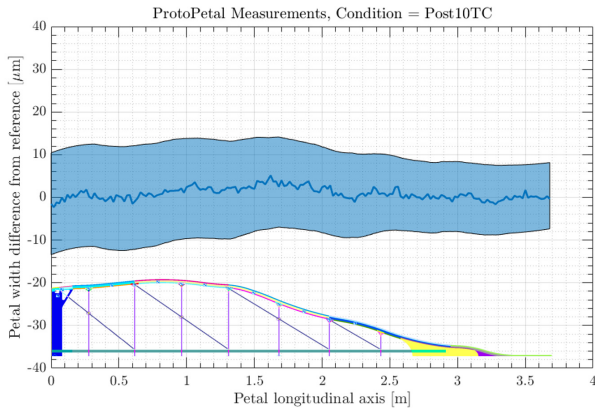


Figure 34: Contrast change from nominal as a function of petal-width bias for flight-design, validated FEM predicts, including worst-case assumptions on material CTEs and temperature uncertainty.

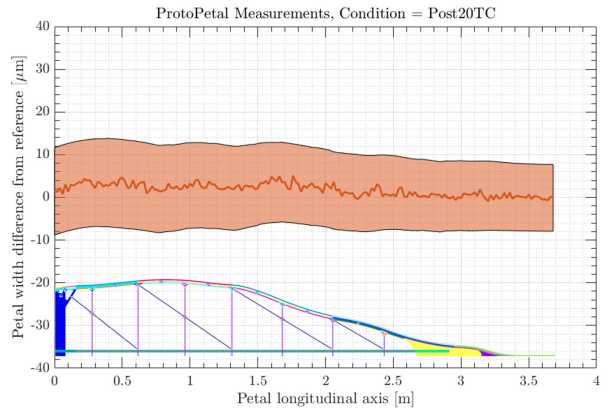
## Summary of Simulation Results

The results of these simulations demonstrate that the petal-width bias, as calculated by the median of the petal-width thermal strain, excluding the petal tip, is an accurate metric of contrast performance due to petal on-orbit thermal deformations. We validated this metric with simulations, including FEM and simulated cases against a reference curve, the change in instrument contrast for a perfect petal-width bias, which has uniform petal-width strain. The uncertainty in the prediction for our cases of interest is 1.2 ppm. This uncertainty is due to the thermal strain variations about the petal-width bias of the midspans (ripples) and the tip.

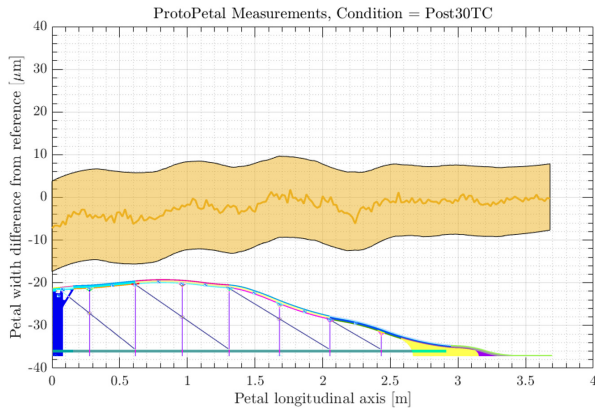
## D Measurement Results: Width Change from Reference



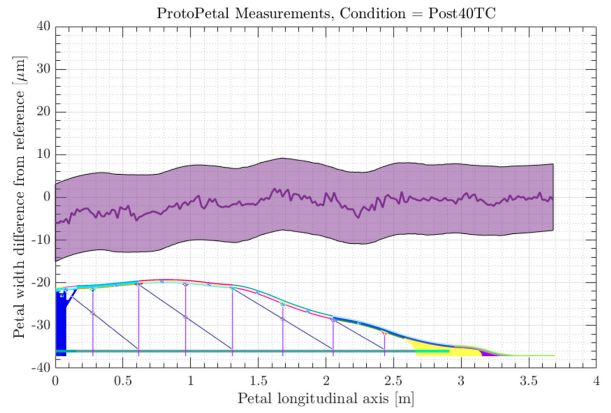
(a) Post 10 thermal cycles.



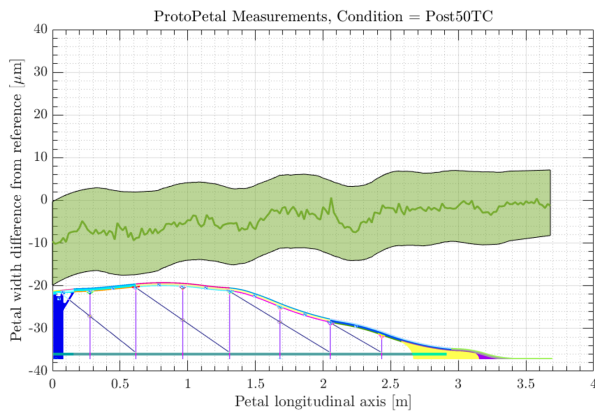
(b) Post 20 thermal cycles.



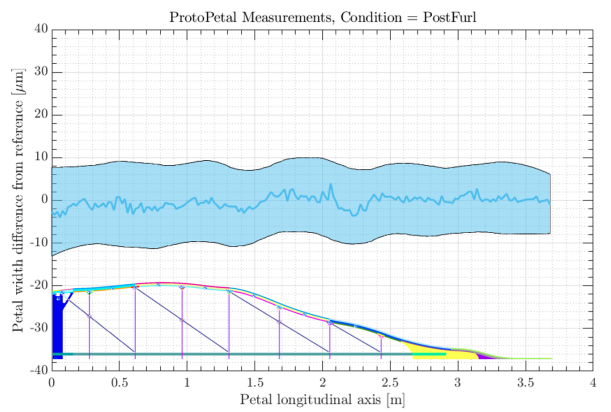
(c) Post 30 thermal cycles.



(d) Post 40 thermal cycles.



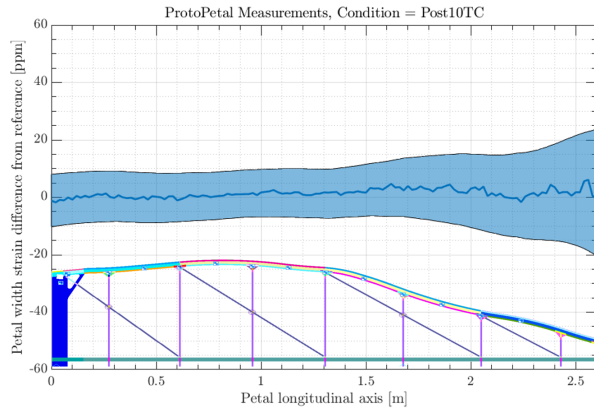
(e) Post 50 thermal cycles.



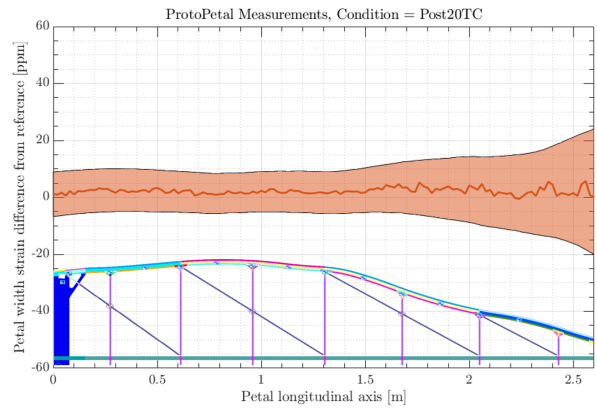
(f) Post 5 furls.

Figure 35: Petal width change from reference for the six measured conditions for milestone 5A. The colors are consistent with the results plotted in Figure 15 and Figure 16.

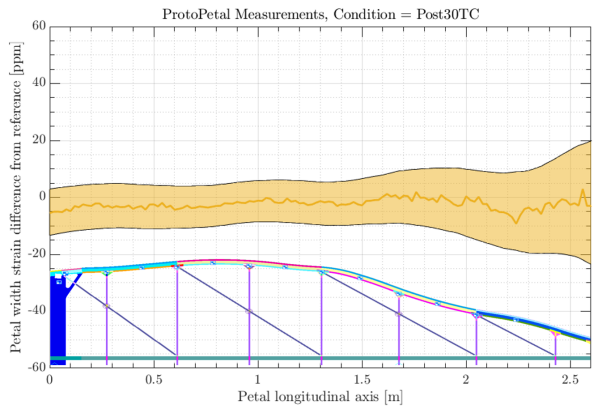
## E Measurement Results: Width Strain from Reference



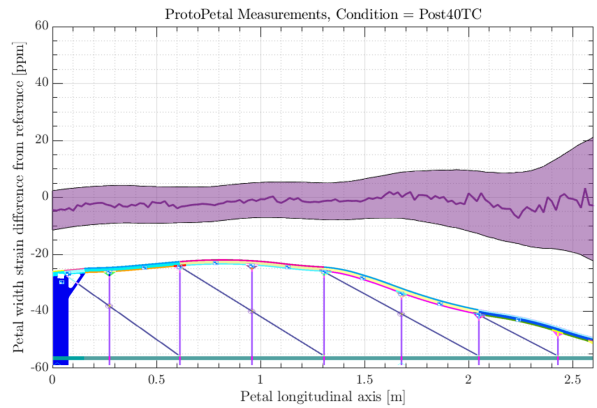
(a) Post 10 thermal cycles. Petal-width bias = 1.3 ppm.



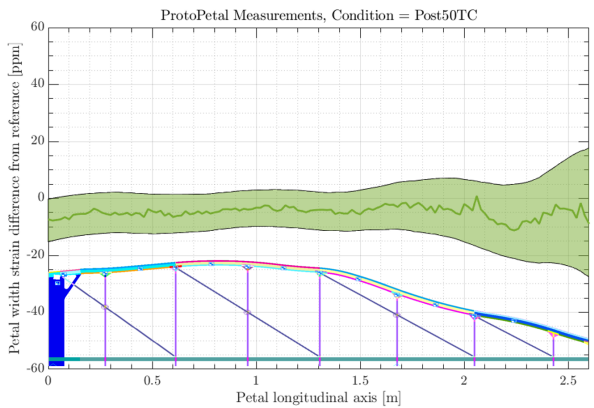
(b) Post 20 thermal cycles. Petal-width bias = 2.1 ppm.



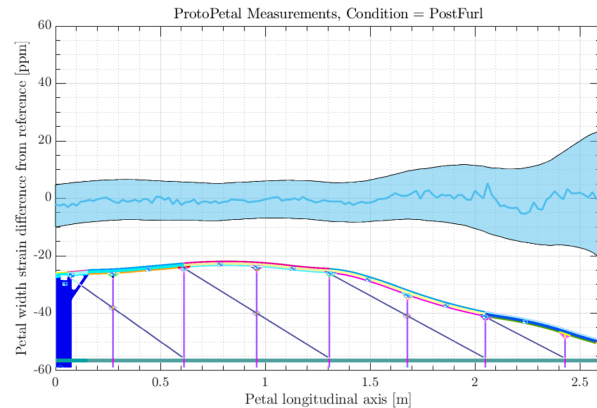
(c) Post 30 thermal cycles. Petal-width bias = -2.4 ppm.



(d) Post 40 thermal cycles. Petal-width bias = -1.6 ppm.



(e) Post 50 thermal cycles. Petal-width bias = -4.5 ppm.



(f) Post 5 furls. Petal-width bias = -0.5 ppm.

Figure 36: Petal width strain from reference for the six measured conditions for milestone 5A. The colors are consistent with the results plotted in Figure 15 and Figure 16.